Effects of pore scale and conjugate heat transfer on thermal convection in porous media

David Korba[1,2], Like Li[1,2,†]

[1] Department of Mechanical Engineering, Mississippi State University, Mississippi State, MS 39762, USA
[2] Center for Advanced Vehicular Systems, Mississippi State University, Mississippi State, MS 39762, USA

[†]Corresponding author: likeli@me.msstate.edu

Abstract

The study of thermal convection in porous media is of both fundamental and practical interest. Typically, numerical studies have relied on the volume-averaged Darcy–Oberbeck–Boussinesq (DOB) equations, where convection dynamics are assumed to be controlled solely by the Rayleigh number (*Ra*). Nusselt numbers (*Nu*) from these models predict *Nu*-*Ra* scaling exponents of 0.9-0.95. However, experiments and direct numerical simulations (DNS) have suggested scaling exponents as low as 0.319. Recent findings for solutal convection between DNS and DOB models have demonstrated that the "pore scale parameters" not captured by the DOB equations greatly influence convection. Thermal convection also has the additional complication of different thermal transport properties (e.g., solid-to-fluid thermal conductivity ratio k_s/k_f and heat capacity ratio σ) in different phases. Thus, in this work we compare results for thermal convection from the DNS and DOB equations. On the effects of pore size, DNS results show that *Nu* increases as pore size decreases. Mega-plumes are also found to be more frequent and smaller for reduced pore sizes. On the effects of conjugate heat transfer, two groups of cases (Group 1 with varying k_s/k_f at $\sigma = 1$ and Group 2 with varying σ at $k_s/k_f = 1$) are examined to compare the *Nu*-*Ra* relations at different porosity (ϕ) and k_s/k_f and σ values. Furthermore, we report that the boundary layer thickness is determined by the pore size in DNS results, while by both the Rayleigh number and the effective heat capacity ratio, $\bar{\phi} = \phi + (1-\phi)\sigma$, in the DOB model.

Key words: convection in porous media, plumes/thermals, buoyant boundary layers

I. Introduction

Thermally driven convection is ubiquitous in nature and industrial processes. Rayleigh–Bénard convection (RBC) is a classical paradigm to study such phenomenon, in which buoyancy-

driven flow is induced in a pure fluid layer due to heating from below and cooling from above. RBC has been studied extensively in past decades (Ahlers, Grossmann, & Lohse 2009; Chillà & Schumacher 2012; Lohse & Xia 2010; Siggia 1994) due to the omnipresence of buoyancy-driven convection in nature and technology. Two dimensionless parameters are standardly used to characterize RBC: (i) pure-fluid Rayleigh number (Ra_f) which describes the ratio of buoyant to viscous forces and (ii) Prandtl number (Pr) which is the ratio of momentum and thermal diffusivity. A third parameter, Γ, defines the aspect ratio of the convection cell. The main response of the system is the fluidic Nusselt number (Nu_f), which describes the efficiency of heat transfer and is defined as the ratio of the total heat transfer rate (conduction and convection) to the conductive heat transfer rate at a wall surface. For very high Rayleigh numbers, there exists an asymptotic regime, where the relationship between Ra_f and Nu_f can typically be described through a constant power law. Considerable literature has been devoted to studying this regime, including several numerical (Iyer *et al.* 2020; Li *et al.* 2021; Toppaladoddi, Succi, & Wettlaufer 2017; Zhu *et al.* 2017, 2018) and experimental (He *et al.* 2012b, 2012a; Niemela *et al.* 2000; Roche *et al.* 2001; Tummers & Steunebrink 2019; Zhang *et al.* 2018) studies.

The analogous problem of thermally (also solutally) driven convection in porous media has begun to receive increasing attention due to its prevalence in assorted domains. Some well-known examples include heat transfer in volcanic rock systems (Ratouis & Zarrouk 2016), subseafloor thermohaline convection (Wilson & Ruppel 2007), sequestration of carbon dioxide (Cinar, Riaz, & Tchelepi 2009; De Paoli, Zonta, & Soldati 2016; Hassanzadeh, Pooladi-Darvish, & Keith 2012), and hydrothermal convection needed for extraction of geothermal energy (Gasparini & Mantovani 1984). Several experimental, analytical, and numerical studies (Hewitt 2020; Hewitt, Neufeld, & Lister 2012, 2013, 2014; Jonsson & Catton 1985; Keene & Goldstein 2015; Kladias & Prasad 1991; Liang *et al.* 2018; Liu *et al.* 2020; Otero *et al.* 2004; Wen, Corson, & Chini 2015) have been devoted to characterizing the corresponding convective behavior and its governing parameters. Like that of RBC, a Rayleigh-Darcy number, commonly referred to as just the Rayleigh number (Ra), is typically used instead as the governing parameter and studied in relation to a porous medium Nusselt (Nu) number. Conventionally, five regimes have been used to describe this type of convection as a function of Ra (Nield & Bejan 2017):

I. the conduction-only regime [$0 \leq Ra \leq 4\pi^2$];

II. the steady state regime [$4\pi^2 \leq Ra \leq 350$];

III. the quasi-periodic regime [$350 \leq Ra \leq 1300$];

IV. the high Rayleigh regime [$1300 \leq Ra \leq 10\ 000$], a turbulent regime that lacks large coherent structures; and

V. the ultimate Rayleigh regime [$Ra > 10\ 000$], similar to the high Rayleigh regime but differing in that the inner flow field becomes self-organized with an interior mega-plume region separated by thin micro-plumic regions close to the bounding wall.

Experiments by Keene and Goldstein (Keene & Goldstein 2015) and Kladias and Prasad (Kladias & Prasad 1991) have further shown that a constant power law regime is present in porous convection at very high *Ra*, suggesting that the presence of the solid phase appears to be nullified. Various authors have suggested power law relationships between *Nu* and *Ra* in the form $Nu \propto Ra^{b}$ for this regime, where *b* is a constant scaling exponent. Based on experiments with compressed argon and polypropylene spheres, Keene and Goldstein proposed $b = 0.319$ for $Ra > 7470$. Lister (Lister 1990) studied convection with water and carbon fibers, suggesting a scaling exponent of 0.33 for high *Ra*. Davidson et al. (Davidson, Kulacki, & Savela 2009) performed experiments on a water-saturated carbon foam. They also included the Prandtl number and the ratio of effective-to-fluid thermal conductivity, k_m/k_f, in their *Nu*-*Ra* relation as $Nu = (0.008 \pm 0.003)\left(k_m/k_f\right)^{0.25\pm0.04} Ra^{0.50\pm0.02}\,\mathrm{Pr}^{0.38\pm0.04}$. It is also pointed out that the magnitude of *Nu* from the above-mentioned experiments have been quite scattered, varying up to an order of magnitude at some Rayleigh numbers.

Up to this point, theoretical and numerical studies for porous media convection have largely relied on macroscopic models; in particular, the Darcy–Oberbeck–Boussinesq (DOB) equations (Nield & Bejan 2017) have been widely adopted for both thermal and solutal convection. In contrast to experimental studies, *Nu*-*Ra* relations obtained from these macroscopic models predict much higher scaling exponents in the range of 0.9-0.95. Otero et al. (Otero *et al.* 2004) used the DOB equations to develop a fit of $Nu \propto Ra^{0.90}$. Hewitt et al. (Hewitt *et al.* 2012) performed simulations based on the DOB equations up to $Ra = 50\ 000$. They recommended $b = 0.95$ as a scaling exponent. Using the same formulation, Kränzien and Jin (Kränzien & Jin 2018) found that a simple linear fit may be more appropriate as $Nu = 0.076Ra + 0.935$. While sparse, some authors have studied thermal and solutal convection in the presence of a porous medium with pore-resolved direct numerical simulations (DNS). Liu et al. (Liu *et al.* 2020) recently performed a two-dimensional (2D) DNS of thermal convection in a square domain with circular objects. They

showed that the relationship between *Nu* and the porosity ϕ was non-monotonic due to the interplay of two competing forces: an increase in heat transfer due to the flow coherence vs. an increase in flow impedance with the addition of the solid array. They also demonstrated asymptotic behavior of *Nu* at high *Ra* numbers, suggesting a relation based on the unconfined fluid Rayleigh and Nusselt number: $Nu_f \propto Ra_f^{0.30}$. Their results presented on the *Nu-Ra* scale matched well with the *b* = 0.319 scaling coefficient by Keene and Goldstein (Keene & Goldstein 2015), however, the magnitude of *Nu* did not show as large of a variance as demonstrated by experiments. A possible reason for this is that Liu et al. only considered a special case with solid-to-fluid thermal conductivity ratio $k_s/k_f = 1$, while in the experiments in (Keene & Goldstein 2015; Kladias & Prasad 1991) it ranged from ~0.33 up to ~321.

A few authors have also directly compared pore-resolved DNS to results obtained from the DOB equations. Karani and Huber (Karani & Huber 2017) performed such a comparison for heat transfer at low Rayleigh numbers (*Ra* < 200), finding that the DOB equations were not able to capture the onset of convection when $k_s/k_f \neq 1$. Gasow et al. (Gasow *et al.* 2020) recently performed a numerical comparison between the DOB equations and pore-resolved DNS for mass transfer. They found that the boundary layer thickness was determined by the pore size instead of the Rayleigh number, and that DNS results predicted a non-linear scaling between the Sherwood and Rayleigh number (analogous to *Nu-Ra* for heat transfer). They concluded that "pore-scale parameters" not captured in the DOB equations played a large role in the convection dynamics, thus suggesting the need for an extension or improvement of the standard DOB equations. While focused on mass transfer, Gasow et al. noted that similar investigation is needed for heat transfer due to the addition of conjugate heat transfer between fluid and solid phases, which was absent in their study. To the best of our knowledge, a comparison of DOB simulations and DNS for thermal convection in porous media with differing thermal transport properties in each phase for high *Ra* (above 200) has not been performed. With the large variation in results obtained with the DOB equations and those from pore-resolved simulations and experiments, two questions arise:

(1) Under what range of conditions are the assumptions used in deriving the DOB equations valid for thermal convection? and

(2) To what extent do conjugate heat transfer and pore size affect the dynamics of thermal convection at higher *Ra*?

Thus, the objective of this study is aiming at answering these questions by performing pore-resolved DNS on a simplified 2D domain and comparing to results from corresponding DOB simulations. We exclusively use the lattice Boltzmann method (LBM) for all simulations, considering Rayleigh numbers up to 50 000.

It is noted that while an actual physical system is in fact three-dimensional (3D), due to the requirement of high resolution and the need to study a wide range of parameters, we employ a simplified 2D configuration. A detailed investigation by van der Poel et al. (Poel, Stevens, & Lohse 2013) for RBC found that 2D and 3D simulations predicted similar Nusselt numbers for high *Pr*. Hewitt et al. (Hewitt *et al.* 2014) also performed 3D simulations using the DOB equations, finding that *Nu* was ~40% larger at high *Ra* in 3D when compared to 2D results. Nonetheless, the scaling coefficient that best fit 3D data was reported as 0.94, compared to 0.95 from 2D simulations performed by the same group. While some discrepancy is expected between 2D and 3D results, we expect the dynamics observed in 2D simulations to be comparable and conclusions made regarding the comparison of DNS and DOB simulations to be valid for 3D cases.

The remainder of this paper is organized as follows. The mathematical formulation for both pore-resolved and macroscopic models are described in detail in Section II, and the corresponding numerical methods in Section III. The validation of the numerical models is shown in Section IV. We then present the simulation results in Section V, focusing on the effects of pore size, conjugate heat transfer, and porosity on the plume dynamics, flow structure, *Nu*-*Ra* relations, and boundary layer thickness. We summarize our findings and discuss future work in Section VI. And Appendix A and Appendix B provide additional information on numerical validation and instantaneous temperature fields, respectively, while the Supplementary materials provide the links to the videos showing the evolution of the temperature fields from the specified initial conditions to statistically steady states for both representative DOB and DNS results.

II. Mathematical formulation

A. Pore scale DNS

We consider a 2D fluid saturated porous medium with square solid blocks as shown in **Figure 1**. The enclosure has an aspect ratio, Γ, of 2 where Γ = Length(L)/Height(H). The dimensions of the blocks are $d \times d$ and the representative elementary volume (REV) has size $m \times m$. The porosity of the domain, ϕ, is uniquely determined by the ratio d/m as

$$\phi = 1 - \left(\frac{d}{m}\right)^2 \tag{1}$$

For this work, we consider three REV sizes as H/m = 10, 25, and 50. It is pointed out that varying H/m (at a fixed ϕ) is representative of varying the pore size within the medium (Gasow *et al.* 2020). The Boussinesq fluid is heated from below and cooled from above with temperatures T_0 and T_1 at the bottom and top walls, respectively. Periodic boundary conditions are employed on the vertical sides for both the flow and thermal field, and no-slip boundary conditions are imposed on all solid surfaces. Conjugate heat transfer is considered at the fluid-solid interface of the square blocks as

$$T_f = T_s \tag{2}$$

$$\mathbf{n}\cdot\left(k\nabla T\right)_f = \mathbf{n}\cdot\left(k\nabla T\right)_s \tag{3}$$

where T is the temperature, k the thermal conductivity, the f and s subscripts denote the fluid and solid phases, respectively, and $\mathbf{n}$ is the unit normal vector to the fluid-solid interface.

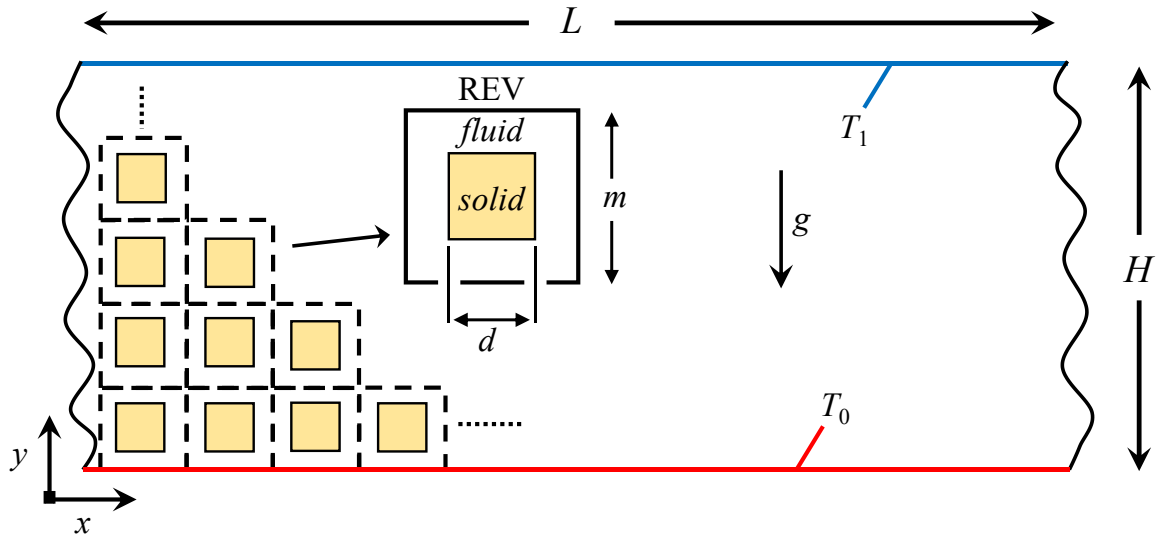

Figure 1: Schematic of porous domain used in direct numerical simulations.

For the fluid phase, the governing equations for DNS are the Navier-Stokes equations (using the Boussinesq approximation) and the energy equation:

$$\nabla\cdot\mathbf{u} = 0 \tag{4}$$

$$\partial_t\left(\mathbf{u}\right) + \left(\mathbf{u}\cdot\nabla\right)\mathbf{u} = -\frac{1}{\rho}\nabla P + \nu_f\nabla^2\left(\mathbf{u}\right) + \mathbf{g}\beta\left(T - T_{ref}\right) \tag{5}$$

$$\left(\rho c_p\right)_f \partial_t\left(T_f\right)+\nabla\cdot\left[\left(\rho c_p\right)_f \mathbf{u}T_f\right]=\nabla\cdot\left(k_f\nabla T_f\right) \tag{6}$$

where $\mathbf{u}$ is the velocity vector, ρ the density, P the pressure, ν the kinematic viscosity, $\mathbf{g}$ the gravitational vector, β the thermal expansion coefficient, T_{ref} a reference temperature taken as $T_{\text{ref}} = (T_0 + T_1)/2$, and c_p the specific heat. For the solid phase, the energy equation reduces to

$$\left(\rho c_p\right)_s \partial_t\left(T_s\right)=\nabla\cdot\left(k_s\nabla T_s\right) \tag{7}$$

Using the reference length H, reference velocity $u_{\text{ref}} = g\beta\Delta TK/\nu$, reference time $t_{\text{ref}} = H/u_{\text{ref}}$, and characteristic temperature difference $\Delta T = T_0 - T_1$ Eqns. (4-7) can be written in dimensionless form as

$$\tilde{\nabla}\cdot\tilde{\mathbf{u}}=0 \tag{8}$$

$$\partial_{\tilde{t}}\left(\tilde{\mathbf{u}}\right)+\left(\tilde{\mathbf{u}}\cdot\tilde{\nabla}\right)\tilde{\mathbf{u}}=-\tilde{\nabla}\tilde{P}+\frac{\text{Pr}}{Ra_f Da}\tilde{\nabla}^2\left(\tilde{\mathbf{u}}\right)+\frac{\text{Pr}}{Ra_f Da^2}z_i\tilde{T} \tag{9}$$

$$\partial_{\tilde{t}}\left(\tilde{T}_f\right)+\tilde{\nabla}\cdot\left(\tilde{\mathbf{u}}\tilde{T}_f\right)=\frac{1}{Ra_f Da}\tilde{\nabla}^2\left(\tilde{T}_f\right) \tag{10}$$

$$\partial_{\tilde{t}}\left(\tilde{T}_s\right)=\frac{\gamma}{Ra_f Da}\tilde{\nabla}^2\left(\tilde{T}_s\right) \tag{11}$$

where $\tilde{}$ denotes a dimensionless value, $\tilde{\nabla}=H\nabla$, $\tilde{T}=T/\Delta T$, and the following dimensionless variables are defined:

$$\begin{gathered}\text{Pr}=\frac{\nu_f}{\alpha_f},\ Ra_f=\frac{H^3\beta\Delta Tg}{\nu_f\alpha_f},\ Da=\frac{K}{H^2},\ \alpha=\frac{k}{\rho c_p}\\ \sigma=\frac{\left(\rho c_p\right)_s}{\left(\rho c_p\right)_f},\gamma=\frac{\alpha_s}{\alpha_f},\text{ and }\frac{k_s}{k_f}=\gamma\sigma\end{gathered} \tag{12}$$

where Pr is the Prandtl number, Ra_f the Rayleigh number for unconfined fluid flow, Da the Darcy number, K the permeability, σ the heat capacity ratio, and γ the thermal diffusivity ratio. It should be noted that while only γ is present in the governing equations (8-11), the conductivity ratio k_s/k_f shows up in the conjugate conditions (Eqs. (2-3)). We define the Nusselt number as the ratio of total heat transfer rate (convective and conductive), $\dot{Q}_{total}$, to purely conductive heat transfer rate, $\dot{Q}_{cond}$, at statistically steady state on the wall as

$$Nu = \frac{\dot{Q}_{total}}{\dot{Q}_{cond}} = \frac{\int_w k\overline{\frac{\partial \tilde{T}}{\partial \tilde{y}}}dA}{\int_w \left(k\overline{\frac{\partial \tilde{T}}{\partial \tilde{y}}}dA \right)\Big|_{Ra_f=0}} \tag{13}$$

where the subscript *w* represents either the top or bottom wall and the $\overline{\ }$ symbol denotes the time-averaged value.

B. Continuum scale DOB equations

For the continuum scale, we begin with volume-averaging of Eqs. (4) and (5) following the "Brinkman-Forchheimer" equation in (Nield & Bejan 2017) for an incompressible fluid with the buoyancy force represented by the Boussinesq approximation:

$$\nabla \cdot \left(\phi \langle \mathbf{u} \rangle \right) = 0 \tag{14}$$

$$\begin{aligned} &\partial_t \left(\phi \langle \mathbf{u} \rangle \right) + \nabla \cdot \left(\phi \langle \breve{\mathbf{u}} \breve{\mathbf{u}} \rangle \right) + \phi \langle \mathbf{u} \rangle \cdot \nabla \langle \mathbf{u} \rangle = \\ &\qquad -\nabla \phi \langle P \rangle + \nu_f \nabla^2 \left(\phi \langle \mathbf{u} \rangle \right) + \phi \mathbf{g} \beta \left(\langle T \rangle - T_{ref} \right) - \frac{\phi^2 \nu_f}{K} \langle \mathbf{u} \rangle - \frac{\phi^3 c_F \rho}{\sqrt{K}} \left| \langle \mathbf{u} \rangle \right| \langle \mathbf{u} \rangle \end{aligned} \tag{15}$$

The last two terms in Eq. (15) denote the Darcy and Forchheimer drag components and $\nabla \cdot \left(\phi \langle \breve{\mathbf{u}} \breve{\mathbf{u}} \rangle \right)$ denotes the momentum dispersion. The drag terms appear from the volume-averaging process (de Lemos 2012) and represent the total drag force per unit volume due to the existence of the porous medium. The <·> symbol represents volume-averaged quantities and the ˘ symbol denotes the fluctuating fields with respect to the averaged value of the local field for the fluid phase (Gasow *et al.* 2020; Karani *et al.* 2017). It is noted here that the above is equivalent to the formulation in (Gasow *et al.* 2020). Under the assumption of local thermal equilibrium, the volume-averaged energy balance equation becomes

$$\left(\rho c_p \right)_m \partial_t \left(\langle T \rangle \right) + \left(\rho c_p \right)_f \nabla \cdot \left(\phi \langle \mathbf{u} \rangle \langle T \rangle \right) + \left(\rho c_p \right)_f \nabla \cdot \left(\phi \left\langle \breve{\mathbf{u}} \breve{T} \right\rangle^f \right) = k_m \nabla^2 \langle T \rangle \tag{16}$$

where k_m is an effective thermal conductivity, $(\rho c_p)_m$ is the overall specific heat capacity with $\left(\rho c_p \right)_m = \phi \left(\rho c_p \right)_f + (1-\phi) \left(\rho c_p \right)_s$, and $\left(\rho c_p \right)_f \nabla \cdot \left(\phi \left\langle \breve{\mathbf{u}} \breve{T} \right\rangle^f \right)$ is the thermal dispersion term (Gasow *et al.* 2020; Karani *et al.* 2017). The $\langle \cdot \rangle^f$ operator (with superscript *f*) denotes volume-

averaging over only the fluid phase. Assuming that thermal dispersion and momentum dispersion are negligible and introducing the additional dimensionless variables

$$Ra = \frac{H\beta\Delta TgK}{\nu_f \alpha_m},\ \zeta = \frac{\alpha_m}{\alpha_f},\ \ \bar{\phi} = \frac{\left(\rho c_p\right)_m}{\left(\rho c_p\right)_f} = \phi + (1-\phi)\sigma\,, \tag{17}$$

Eqs. (14-16) can be rewritten as

$$\hat{\nabla}\cdot\hat{\mathbf{u}} = 0 \tag{18}$$

$$\partial_{\hat{t}}\left(\hat{\mathbf{u}}\right) + \hat{\mathbf{u}}\cdot\hat{\nabla}\left(\hat{\mathbf{u}}/\phi\right) = -\frac{1}{\rho}\hat{\nabla}\phi\hat{P} + \frac{\mathrm{Pr}}{\zeta Ra}\hat{\nabla}^2\left(\hat{\mathbf{u}}\right) + \frac{\phi\,\mathrm{Pr}}{\zeta RaDa}\hat{T}z_i - \frac{\phi\,\mathrm{Pr}}{\zeta RaDa}\hat{\mathbf{u}} - \frac{\phi c_F}{\sqrt{Da}}\left|\hat{\mathbf{u}}\right|\hat{\mathbf{u}} \tag{19}$$

$$\partial_{\hat{t}}\left(\hat{T}\right) + \hat{\nabla}\cdot\left(\frac{\hat{\mathbf{u}}\hat{T}}{\bar{\phi}}\right) = \frac{1}{Ra}\hat{\nabla}^2\left(\hat{T}\right) \tag{20}$$

where $Ra = Ra_f Da/\zeta$ is the Rayleigh number for the porous medium, $\alpha_m = k_m/\left(\rho c_p\right)_m$ the effective thermal diffusivity, ζ the ratio between α_m and α_f, $\bar{\phi}$ the ratio between the overall heat capacity and that of the fluid, and z_i is the ith component of the unit vector in the gravity direction. The symbol ^ represents dimensionless volume-averaged quantities and $\hat{\mathbf{u}} = \phi\langle\mathbf{u}\rangle$ is the superficial velocity (also called Darcy velocity). With the assumption that $Da \ll 1$, the DOB equations are obtained:

$$\hat{\nabla}\cdot\hat{\mathbf{u}} = 0 \tag{21}$$

$$\hat{\nabla}\hat{P}_n = -\hat{\mathbf{u}} + z_i\hat{T} \tag{22}$$

$$\partial_{\hat{t}}\hat{T} + \hat{\nabla}\cdot\left(\frac{\hat{\mathbf{u}}\hat{T}}{\bar{\phi}}\right) = \frac{1}{Ra}\hat{\nabla}^2\hat{T} \tag{23}$$

Where $\hat{P}_n = RaDa\langle p\rangle/\zeta\,\mathrm{Pr}$ is a normalized pressure. Equations (21-23) are the same as the traditional DOB equations used for macroscopic-level studies (Gasow *et al.* 2020; Hewitt 2020; Hewitt *et al.* 2012, 2013, 2014; Karani & Huber 2017; Kränzien & Jin 2018; Nield & Bejan 2017; Otero *et al.* 2004; Wen *et al.* 2015).

An important distinction on the definition of *Ra* and Eq. (23) is made here in comparison with previous studies for thermal convection. Some authors (Karani *et al.* 2017; Karani & Huber

2017; Le Reun & Hewitt 2021; Qiang *et al.* 2021) have posed the effective thermal diffusivity, α_m, instead as $k_m/(\rho c_p)_f$ and introduced a modified dimensionless time $\hat{t}/\bar{\phi}$. In doing so, Eq. (23) is instead re-written as

$$\frac{\partial \hat{T}}{\partial(\hat{t}/\bar{\phi})} + \hat{\nabla}\cdot(\hat{\mathbf{u}}\hat{T}) = \frac{\nu_f}{H\beta\Delta TgK}\frac{k_m}{(\rho c_p)_f}\hat{\nabla}^2\hat{T} = \frac{\bar{\phi}}{Ra}\hat{\nabla}^2\hat{T}. \tag{24}$$

Following this modified formulation, one notices that the effects of the heat capacity ratio σ does not explicitly enter the statistically steady problem and the effect of different thermal transport properties enter through only the thermal conductivity ratio, k_s/k_f, in the Rayleigh number. To demonstrate the effects of both the heat capacity ratio and the thermal conductivity ratio in DOB simulations, we follow the formulation and definitions presented in Eqs. (17, 21-23). As such, the effects of conjugate heat transfer are considered through the effective thermal conductivity k_m in *Ra* and the heat capacity ratio σ in $\bar{\phi}$.

It is also pointed out that in deriving Eqs. (21-23), additional assumptions were employed including that the thermal non-equilibrium between the two phases is small, and the terms on the order of $O(1/Da)$ dominate in the momentum equation. Further implications of these will be discussed in the succeeding sections. To compare pore- to continuum-scale formulations, we define the following Nusselt number for DOB simulations following (Gasow et al., 2020) with A_w the wall surface area:

$$Nu = \frac{\int_w \overline{\frac{\partial \hat{T}}{\partial \hat{y}}} dA}{A_w} \tag{25}$$

It should be noted that the *Nu* definitions in Eqs. (13) and (25) are equivalent and analogous to the Sherwood number definitions in previous DNS and DOB studies for mass transfer (Gasow et al., 2020).

III. Numerical method

In recent years, the lattice Boltzmann method has gained significant attention in simulating complex fluid flow and transport problems, largely due to its kinetic nature, simple implementation, ease of parallelization, and intrinsic relations between microscopic distribution

functions (DFs) and macroscopic properties (Aidun & Clausen 2010; Benzi, Succi, & Vergassola 1992; Chen & Doolen 1998; He & Luo 1997; Li, Mei, & Klausner 2013; Li *et al.* 2014; Yoshida & Nagaoka 2010; Yu *et al.* 2003). With these inherent advantages and its mesoscopic basis, it is no surprise that the LBM has been widely used in the study of pore-scale dynamics. As such, we use the LBM in this work to solve both the DNS and DOB equations, implemented with in-house developed Fortran 90 code.

A. LBM for pore scale DNS

In solving the pore scale equations, a 2D nine-velocity (D2Q9) multiple relaxation time (MRT) LBM model (Lallemand & Luo 2000; Yu *et al.* 2003) is used to solve the flow field, and a 2D five-velocity (D2Q5) MRT-LBM model (Li, Mei, & Klausner 2017; Yoshida & Nagaoka 2010) is used to solve the temperature field. The LBM models are coupled through the Boussinesq force which is treated as a source term in the D2Q9 model.

a. D2Q9 for fluid flow

For the incompressible flow at the pore scale, the LBM evolution scheme is taken as (Lallemand & Luo 2000; Yu *et al.* 2003)

$$f_i\left(\mathbf{x}+\mathbf{e}_i\delta t, t+\delta t\right) = f_i\left(\mathbf{x},t\right) - \left[\mathbf{M}^{-1}\mathbf{S}\cdot\left(\mathbf{m}-\mathbf{m}^{\mathrm{eq}}\right)\left(\mathbf{x},t\right)\right]_i + \mathbf{F}_i\delta t \tag{26}$$

where $f_i(\mathbf{x}, t)$ ($i = 0 – 8$) are the density distribution functions with a set of discrete velocity vectors $\mathbf{e}_i$ at position $\mathbf{x}$ and time t, $\mathbf{m}$ are the velocity moments, $\mathbf{m}^{\mathrm{eq}}$ are the corresponding equilibrium moments, and $\mathbf{F}_i$ is a force term that can be expressed as $\mathbf{F}_i = -3\omega_i\rho\mathbf{e}_i\cdot\mathbf{F}/c^2$ ($\mathbf{F} = (F_x, F_y)$ is the force vector, ω_i are lattice weights given by $\omega_0 = 4/9$, $\omega_{1\text{-}4} = 1/9$, and $\omega_{5\text{-}8} = 1/36$, and $c = \delta x/\delta t$ is the unit of velocity with δx and δt being the lattice spacing and discrete time step, respectively) (Luo 1993). The force vector is related to the Boussinesq approximation as $\mathbf{F} = (0, \mathbf{g}\beta(T\text{-}T_{\mathrm{ref}}))$. $\mathbf{M}$ is a 9x9 transformation matrix and $\mathbf{S} = \mathbf{M}\tilde{\mathbf{S}}\mathbf{M}^{-1} = \mathrm{diag}(s_0, s_1, \ldots, s_8)$ is a diagonal relaxation matrix ($\tilde{\mathbf{S}}$ is the collision matrix and $s_0, s_1, \ldots, s_8$ are relaxation coefficients). The transformation matrix $\mathbf{M}$ linearly maps the distribution functions $f \in \mathrm{V} \equiv \mathrm{R}^9$(velocity space) to their velocity moments $f \in \mathrm{M} = \mathrm{R}^9$(moment space) by

$$\mathbf{m} = \mathbf{M}\cdot\mathbf{f},\ \mathbf{f} = \mathbf{M}^{-1}\cdot\mathbf{m}, \tag{27}$$

where the nine velocity moments are given by

$$\begin{aligned}\mathbf{m} &= \left(m_0, m_1, m_2, m_3, m_4, m_5, m_6, m_7, m_8\right)^{\dagger} \\ &= \left(\rho, e, \varepsilon, j_x, q_x, j_y, q_y, p_{xx}, p_{xy}\right)^{\dagger}\end{aligned} \tag{28}$$

In the above, m_0 is the fluid density, e is related to energy, ε is related to the energy squared, j_x and j_y are components of the momentum, q_x and q_y are related to the energy flux, and p_{xx} and p_{xy} are the symmetric and traceless components of the strain-rate tensor (Lallemand & Luo 2000; Yu *et al.* 2003). For efficient computation and storage, the LBM evolution equation (25) is solved in two steps:

collision step:

$$\mathbf{f}_i^*\left(\mathbf{x},t\right) = \mathbf{f}_i\left(\mathbf{x},t\right) - \left[\mathbf{M}^{-1}\mathbf{S}\cdot\left(\mathbf{m}-\mathbf{m}^{\mathrm{eq}}\right)\left(\mathbf{x},t\right)\right]_i + \mathbf{F}_i\delta t \tag{29}$$

and *streaming* step:

$$\mathbf{f}_i\left(\mathbf{x}+\mathbf{e}_i\delta t, t+\delta t\right) = \mathbf{f}_i^*\left(\mathbf{x},t\right) \tag{30}$$

where * denotes post-collision values. The macroscopic fluid density and velocity are thus related to the DFs by

$$\rho = \sum_{i=0}^{8} f_i\left(\mathbf{x},t\right) \tag{31}$$

$$\mathbf{u} = \frac{1}{\rho}\sum_{i=0}^{8}\mathbf{e}_i f_i\left(\mathbf{x},t\right) + \frac{\delta t}{2}\mathbf{F}\left(\mathbf{x},t\right). \tag{32}$$

The other details of the matrices **M**, **S**, and equilibrium moments $\mathbf{m}^{(\mathrm{eq})}$ can be found in (Lallemand & Luo 2000; Yu *et al.* 2003). The bounding walls and solid block boundaries are specified halfway between the LBM nodes, thus a standard bounce-back scheme is used to implement the no-slip condition.

b. D2Q5 for heat transfer

To apply the LBM to solve for the temperature field at the pore scale, Eqs. (10) and (11) can be rearranged to a standard convection-diffusion equation (CDE) in the form

$$\frac{\partial\theta}{\partial t} + \nabla\cdot\left(\mathbf{u}\theta\right) = \nabla\cdot\left(D\nabla\theta\right) + G, \tag{33}$$

where θ is the macroscopic scalar variable of interest, such as temperature, D is the diffusion coefficient, and G represents any combination of source terms. The LBM evolution equation for the D2Q5 model is (Li *et al.* 2017; Yoshida & Nagaoka 2010)

$$h_i\left(\mathbf{x}+\mathbf{e}_i\delta t, t+\delta t\right)=h_i^*\left(\mathbf{x},t\right)-\left[\mathbf{M}^{-1}\mathbf{S}\cdot\left(\mathbf{m}-\mathbf{m}^{\mathrm{eq}}\right)\left(\mathbf{x},t\right)\right]_i+\omega_i\delta t G\left(\mathbf{x},t\right), \tag{34}$$

where $h_i(\mathbf{x}, t)$ (i = 0 – 4) are microscopic distribution functions, the lattice weights are given by ω_0=1/3 and $\omega_{1\text{-}4}$=1/6, and the matrix $\mathbf{M}$ maps the DFs to the moment space through $\mathbf{m} = \mathbf{M}\cdot\mathbf{h}$ and $\mathbf{m}^{(\mathrm{eq})} = \mathbf{M}\cdot\mathbf{h}^{(\mathrm{eq})}$. We choose the matrices as in (Yoshida & Nagaoka 2010) and the equilibrium moments can be explicitly obtained as in (Li *et al.* 2013, 2017). In using the LBM for Eqs. (10) and (11), the source term is set to G = 0. Using the set of distribution functions $h_i(\mathbf{x}, t)$, the temperature is obtained from $\theta\left(\mathbf{x},t\right)=\sum_{i=0}^{4}h_i\left(\mathbf{x},t\right)$. The evolution equation is also computationally executed through a collision-streaming procedure:

collision step:

$$h_i^*\left(\mathbf{x},t\right)=h_i\left(\mathbf{x},t\right)-\left[\mathbf{M}^{-1}\mathbf{S}\cdot\left(\mathbf{m}-\mathbf{m}^{\mathrm{eq}}\right)\left(\mathbf{x},t\right)\right]_i+\omega_i\delta t G\left(\mathbf{x},t\right). \tag{35}$$

streaming step:

$$h_i\left(\mathbf{x}+\mathbf{e}_i\delta t, t+\delta t\right)=h_i^*\left(\mathbf{x},t\right). \tag{36}$$

Implementation of the conjugate conditions and outer domain boundary conditions follow (Korba, Wang, & Li 2020; Li *et al.* 2013, 2014) for which the second-order accuracy is preserved for straight boundaries and interfaces.

B. LBM for macroscale DOB equations

a. Streamfunction formulation for fluid flow

Following (Gasow *et al.* 2020; Hewitt *et al.* 2012; Kränzien & Jin 2018), a streamfunction method (SFM) is used to solve the fluid flow in the DOB equations. The streamfunction, ψ, is related to the velocity field by

$$\left(u_x,u_y\right)=\left(\frac{\partial\psi}{\partial y},-\frac{\partial\psi}{\partial x}\right). \tag{37}$$

Taking the curl of the momentum equation (22) with the above relation gives

$$\nabla^2\psi=-\frac{\partial\hat{T}}{\partial\hat{x}} \tag{38}$$

A diffusion coefficient, D_{SF}, is introduced to solve Eq. (38) with the LBM as

$$D_{SF}\nabla^2\psi=G_{SF} \tag{39}$$

where $G_{SF} = -D_{SF}\dfrac{\partial \hat{T}}{\partial \hat{x}}$ can be considered as a source term. It is pointed out that Eqn. (39) is in the form of a standard diffusion equation.

b. D2Q5 for fluid flow and heat transfer

Equations (23) and (39) fit the general form of the CDE in Eq. (33), where the scalar of interest, θ, is either the temperature or the streamfunction. Introducing a set of DFs $g_i(\mathbf{x},t)$ to represent these macroscopic scale quantities, one can obtain the scalar of interest from

$$\theta(\mathbf{x},t) = \sum_{i=0}^{4} g_i(\mathbf{x},t). \tag{40}$$

where the *collision* and *streaming* processes are respectively given by

$$g_i^*(\mathbf{x},t) = \mathbf{g}_i(\mathbf{x},t) - \left[\mathbf{M}^{-1}\mathbf{S}\cdot\left(\mathbf{m}-\mathbf{m}^{\mathrm{eq}}\right)(\mathbf{x},t)\right]_i + \omega_i \delta t G(\mathbf{x},t) \tag{41}$$

and

$$g_i(\mathbf{x}+\mathbf{e}_i\delta t, t+\delta t) = \mathbf{g}_i^*(\mathbf{x},t). \tag{42}$$

The matrices **M**, **S**, and $\mathbf{m}^{(\mathrm{eq})}$ and the lattice weights are the same as in Section III-A-b. In solving the DOB equations, the energy equation is first advanced in time to update the thermal field. Then, Eqn. (39) is solved to update the streamfunction, ψ, where the source term in the LBM model is $G = -D_{SF}\dfrac{\partial \hat{T}}{\partial \hat{x}}$. Finally, the velocity is updated from the gradients of the streamfunction following Eq. (37).

IV. Validation

In this section, the DNS-LBM and DOB-LBM models are implemented to reproduce results of natural convection from other numerical methods. Both mass and heat transfer are studied for pore and continuum scale simulations to demonstrate the applicability and accuracy of the present LBM models. All simulations in this work consider the initial flow field as stationary ($\mathbf{u} = 0$) and the initial temperature field with a magnitude of $(T_0 + T_1)/2 + \lambda$, where λ is an initial perturbation of a random normal distribution between -0.01 and 0.01.

A. DNS and DOB models for mass transfer

Gasow et al. (Gasow *et al.* 2020) performed a similar study as discussed here for mass transfer, thus, we find it valuable to present a comparison to our results obtained from the LBM.

First, the DNS model is reduced to simulate mass transfer, i.e., the conjugate conditions on the fluid-solid interfaces are replaced with non-penetrative boundaries and the fluid energy equation is instead considered with concentration, C, as the transport variable of interest. The Sherwood number (analogous to the Nusselt number) is obtained as

$$Sh = \frac{\int_w \overline{\frac{\partial \tilde{C}}{\partial \tilde{y}}} dA}{\int_w \left(\overline{\frac{\partial \tilde{C}}{\partial \tilde{y}}} dA \right)\Big|_{Ra_f = 0}}. \tag{43}$$

Figure 2 shows the temporal evolution of the horizontally averaged Sherwood numbers (Sh) obtained from DNS for $H/m = 20$ and $\phi = 0.56$ ($m/d = 1.5$) at the Schmidt number $Sc = 1$. The time-averaged Sherwood numbers are $Sh = 36.85$, 59.01, and 92.97 for the respective cases at $Ra = 5000$, 10 000, and 20 000. Good agreement is demonstrated between our LBM results and those from (Gasow *et al.* 2020) . It is pointed out that in this work the time-averaging of the Sherwood number and Nusselt number was performed over a duration of 500 000δt once a statistically steady state was reached (as shown in **Figure 2**).

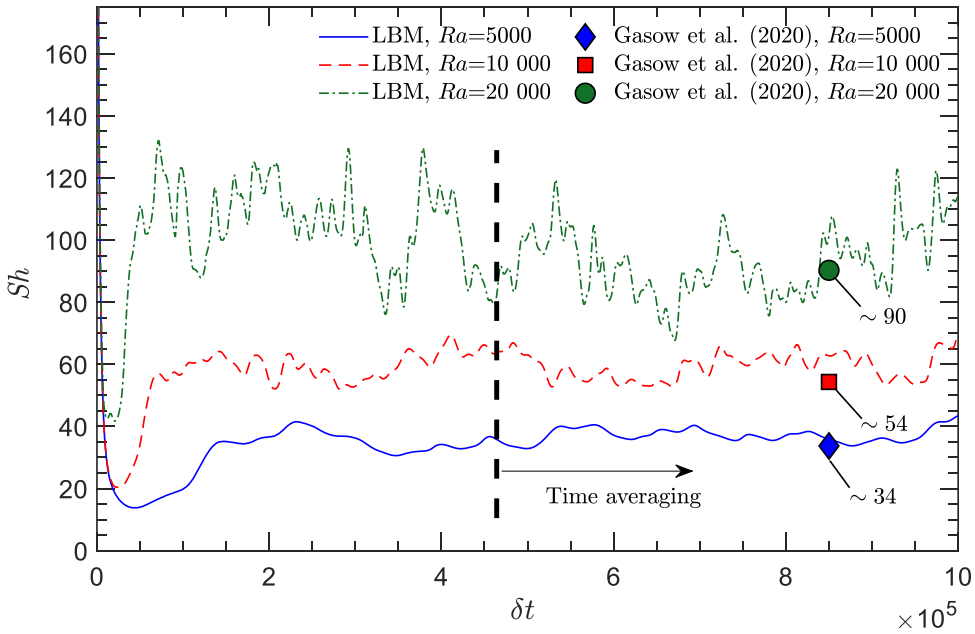

Figure 2: Sherwood number (Sh) versus dimensionless time δt at $Ra = 20\,000$, $Sc = 1$, $H/m = 20$, and $m/d = 1.5$ ($\phi = 0.56$).

In addition, the instantaneous concentration field from the DNS at Ra = 20 000 is provided in Fig. A-1 in Appendix A. Similarly, the macroscale DOB model implemented with the LBM is also applied for mass transfer; and a snapshot of the instantaneous concentration field for the case of Ra = 20 000 is given in Fig. A-2 of Appendix A. Both concentration fields in Figs. A-1 and A-2 demonstrate excellent agreement in plume shape, micro-plumic behavior near the wall, and frequency of vertical plume columns with those shown in (Gasow *et al.* 2020).

B. DNS and DOB modes for heat transfer

Further validation of the DNS-LBM model for heat transfer is performed by comparison with natural convection results obtained by Liu et al. (Liu *et al.* 2020) for a domain (Γ = 1) filled with circular blocks. The referenced study differs from ours in that the side walls are insulated and non-penetrative, and circular obstacles are used instead of squares. In (Liu *et al.* 2020), the effects of porosity in both porous and non-porous media were presented through the use of an immersed boundary method (IBM) in the Euler-Lagrange framework. It is pointed out that Liu et al. considered the Nusselt number based on the fluid thermal conductivity (Miansari *et al.* 2015):

$$Nu_f = \frac{\int_w \overline{\frac{\partial \tilde{T}}{\partial \tilde{y}}} dA}{A_w} \tag{44}$$

Three main points are considered for validation: (1) the Nusselt number for traditional RBC (ϕ = 1) follows an effective power law near $Nu_f \propto Ra_f^{0.3}$ (Iyer *et al.* 2020; Niemela *et al.* 2000; Zhang *et al.* 2017) in the range considered within this work, (2) in the lower Ra_f range (10^6~10^8), an increase in Nu_f is expected as ϕ increases, and (3) in this lower Ra_f range, a steep effective power law $Nu_f \propto Ra_f^{0.65}$ was found for thermal convection in porous media. It is pointed out that Liu et al. assumed thermal properties to be the same in both phases, thus the results presented here only consider σ = 1 and k_s/k_f = 1 for consistency.

The results are compared in **Figure 3**. The effective power law scales and presented trends from our LBM simulations match well with the reported results for non-porous media (ϕ = 1). Furthermore, their predicted effects of porosity on Nu_f are observed with LBM simulations as ϕ is varied. The difference observed at ϕ = 0.75 is attributed to the different solid-block shapes (square vs. circular geometry), boundary conditions imposed on the side walls (periodic vs. no-slip/insulated), and the variation in pore size. Overall, the results agree well, and a distinct

transition from low-*Ra* Darcy-type convection to high-*Ra* convection is present and consistent with Liu *et al.* 2020.

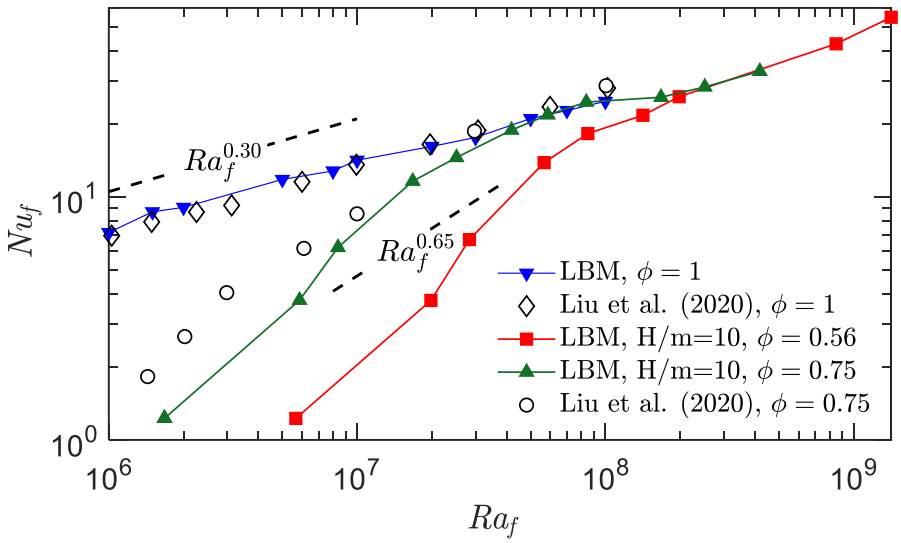

Figure 3: Variations of Nu_f with Ra_f for different ϕ with $Pr = 1$, $\sigma = 1$, and $k_s/k_f = 1$.

The solutions to the DOB equations for thermal convection have been studied with quite a few numerical methods: (1) Hewitt et al. (Hewitt *et al.* 2012) used a stream function method (SFM) where Eq. (39) was solved with a spectral method and Eq. (23) with an alternating direction implicit method, (2) Kränzien and Jin (Kränzien & Jin 2018) solved the SFM-equations with a second-order implicit backward method used for the time discretization and a second-order central-difference scheme used for spatial discretization, (3) Kränzien and Jin used a pressure correction method (PCM) where an intermediate velocity field was determined from the momentum equation and then a corrected pressure term was added to satisfy the continuity equation, and (4) Wen et al. (Wen *et al.* 2015) used a Fourier-Chebyshev pseudospectral method to solve the SFM-based equations. It is noted that the parameters in these studies all used $k_s/k_f = 1$ and $\sigma = 1$. Thus, our SFM-based LBM model is also implemented with these inputs. Corresponding results are summarized in **Figure 4** for each of the above-mentioned methods and our DOB-LBM model. Excellent agreement is observed for the wide range of *Ra* studied, thus we consider the present DOB-LBM model for thermal convection validated.

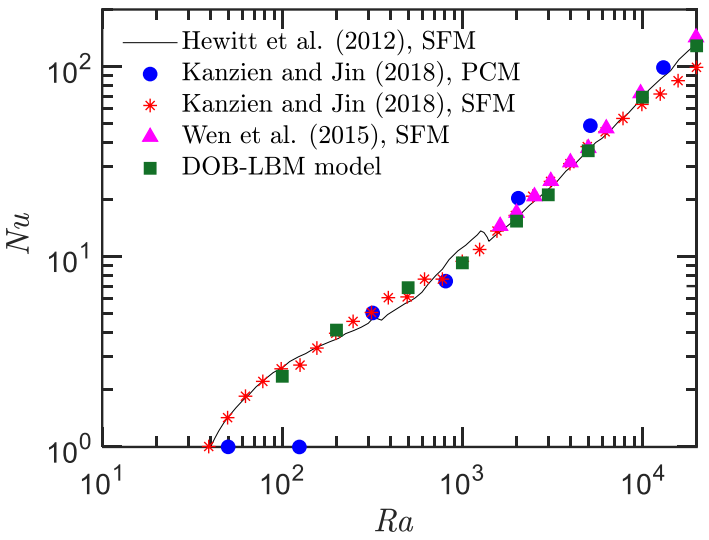

Figure 4: Variations of *Nu* with *Ra* for the case of $\sigma = 1$ and $k_s/k_f = 1$ from DOB simulations.

V. Results and discussion

Table 1 shows the grid resolution used for both DOB and DNS simulations, where N_{rev} is the number of cells within each REV. A mesh independence study was performed for $H/m = 25$ and $Ra = 5000$, where the grid resolution per REV was varied between $N_{rev} = 900$, 1600, 2500, 3025, and 3600. We found that that the variation of Nu was less than 5% for succeeding mesh sizes after $N_{rev} = 2500$, thus we consider $N_{rev} = 2500$ as our minimum mesh resolution. Furthermore, following (Liu *et al.* 2020; Shishkina *et al.* 2010), for RBC the Kolmogorov length scale η can be estimated by $\eta = HPr^{1/2}/[Ra_f(Nu_f - 1)]^{1/4}$ and the Batchelor scale η_B by $\eta_B = \eta Pr^{-1/2}$. At $Ra = 50\,000$, for the highest value Nu_f obtained within this work, the grid spacing remains below ~0.44η and ~$0.44\eta_B$. Therefore, we consider the mesh resolution sufficient. To reduce the complexity of the study we set the Prandtl number to be $Pr = 1$ throughout this work.

Table 1: Details of grid resolutions used in simulations.

	H/m	Ra	$N_x \times N_y$	N_{rev}
DNS	10	$0\text{-}5\times10^4$	900×1800	8100
	25	$0\text{-}5\times10^4$	1500×3000	3600
	50	$0\text{-}5\times10^4$	2500×5000	2500
DOB	-	$0\text{-}5\times10^4$	900×1800	-

A. Permeability and effective thermal conductivity

To compare DNS to DOB results, the permeability, K, was determined by simulating isothermal forced convection in the porous medium. Using this approach, K is determined by the

ratio of an applied pressure gradient to the mean velocity (averaged over both the fluid and solid phase). It is pointed out that the conventional Darcy number, $Da_C = K/d^2$, is defined as the ratio of the permeability to a characteristic length of the solid phase. Thus, Da_C is only dependent upon porosity while $Da = Da_C d^2/H^2$ includes a dependence on both porosity and pore size. The obtained values of Da_C from the permeability study with the LBM are presented in **Table 2**; a comparison to results in (Gasow *et al.* 2020) is also shown demonstrating excellent matching.

Table 2: Main parameters for DOB and DNS models.

m/d	ϕ(porosity)	Da_C (present)	Da_C (Gasow *et al.* 2020)	k_m/k_f (k_s/k_f =0.1)	k_m/k_f (k_s/k_f =10)
1.25	0.36	0.00113	0.0011	0.308	3.232
1.5	0.5556	0.00795	0.0079	0.452	2.378
2	0.75	0.04779	-	0.647	1.538

Furthermore, the stagnant effective thermal conductivity of the porous medium, k_m, is also obtained with the LBM model, where $k_m = (k_f / A_w)\int_w \overline{\frac{\partial \tilde{T}}{\partial \tilde{y}}} dA$ is determined with pure conduction (Ra = 0). It is pointed out that while only k_f is explicitly present in the calculation of k_m since the solid blocks are not touching the upper and lower walls in the considered simulation domain (Fig. 1), the temperature gradient evaluated on the walls depends on both k_s and k_f. It is also worth mentioning that k_m depends on k_s, k_f and the structure of the porous medium and cannot always be assumed as the simple volumetric ($k_m = \phi k_f + (1-\phi) k_s$) or harmonic mean (Karani & Huber 2017; Wang & Pan 2008). Values of k_m/k_f used in this work are shown in **Table 2**. In addition, the variations of the normalized effective thermal conductivity (k_m/k_f) at different porosities are also presented in **Figure 5**. It should be noted that (1) for $k_s/k_f < 1$, k_m/k_f increases as the porosity ϕ increases, while (2) for $k_s/k_f > 1$, k_m/k_f decreases as ϕ increases. One should also notice the similarity in the definition of k_m and that in the denominator of Nu for DNS simulations in Eq. (13). Further implications of these effects are discussed in the following sections.

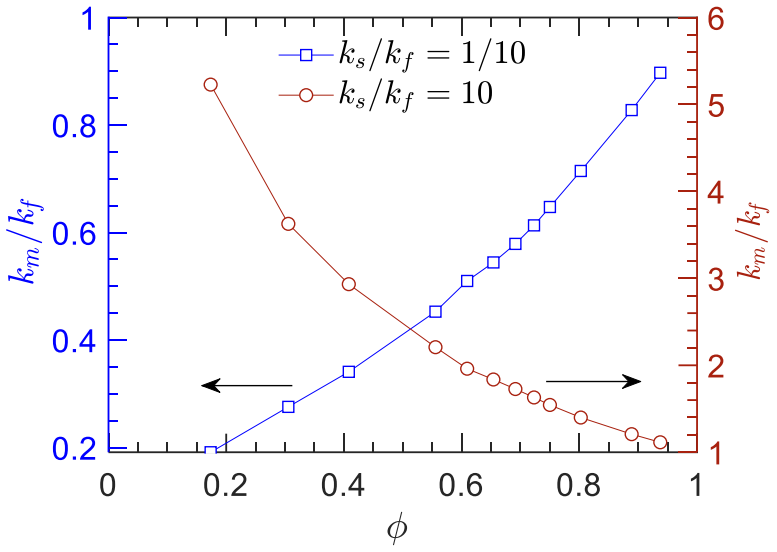

Figure 5: Variation of the normalized effective thermal conductivity (k_m/k_f) with porosity ϕ.

B. Effects of pore size

In this section, the influence of varied solid arrays on the convection dynamics are examined. For this section, we consider only the case with the same thermal transport properties in the two phases (i.e., $k_s/k_f = 1$ and $\sigma = 1$, thus $\gamma = 1$ and $\overline{\phi} = 1$). The effects of different transport properties on thermal convection will be presented in Section V-C. It is stressed that in the present study the conduction within the solid blocks is considered; this is distinct from several previous porescale studies of solutal convection where the solid phase is impermeable.

a. Mega and proto-plumes

Instantaneous volume-averaged temperature fields at Ra = 10 000 obtained from DOB simulations and DNS at $\phi = 0.56$ are shown in **Figure 6** and **Figure 7**, respectively. The volume-averaged temperature fields from DNS are obtained through weighted averaging over the REV as

$$\hat{T}_{rev} = \left(\sum_f \rho c_p \tilde{T} + \sum_s \rho c_p \tilde{T} \right) \Big/ \left(\rho c_p \right)_m .$$

Interestingly, as the pore size is reduced (through increasing H/m), the characteristic width of the interior mega-plumes decreases while the spatial frequency of mega-plumes increases. This behavior is of course absent in RBC and is uncaptured through the DOB equations. It is pointed out that a similar observation was noted by Gasow et al. (Gasow *et al.* 2020) in the study of mass transfer. Furthermore, the results suggest that as the pore size continues to decrease ($H/m \rightarrow \infty$), the DOB simulations will approach those of DNS. In the framework of the DOB equations, a major

assumption is that the terms on the order of $O(1/Da)$ dominate. For $H/m = 10$ with $\phi = 0.56$, the Darcy number is $Da = 3.53\times10^{-5}$, while for $H/m = 50$, $Da = 1.41\times10^{-6}$. Thus, the terms including $1/Da$ (terms considered in DOB equations) are expected to have a contribution of 25 times more for $H/m = 50$ than $H/m = 10$ for the porosity studied here; we believe for this reason a sufficiently small Darcy number is required for DOB and DNS results to have comparable plume development.

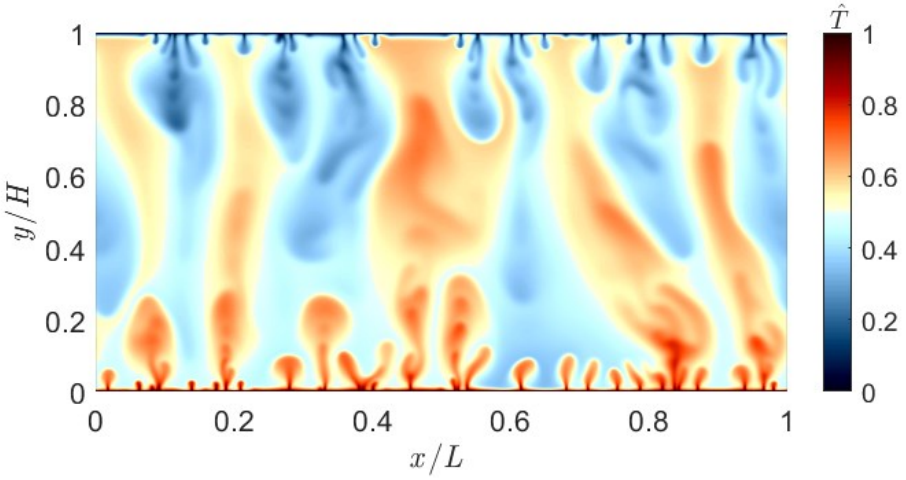

Figure 6: Instantaneous temperature field at *Ra* = 10 000 from DOB simulations.

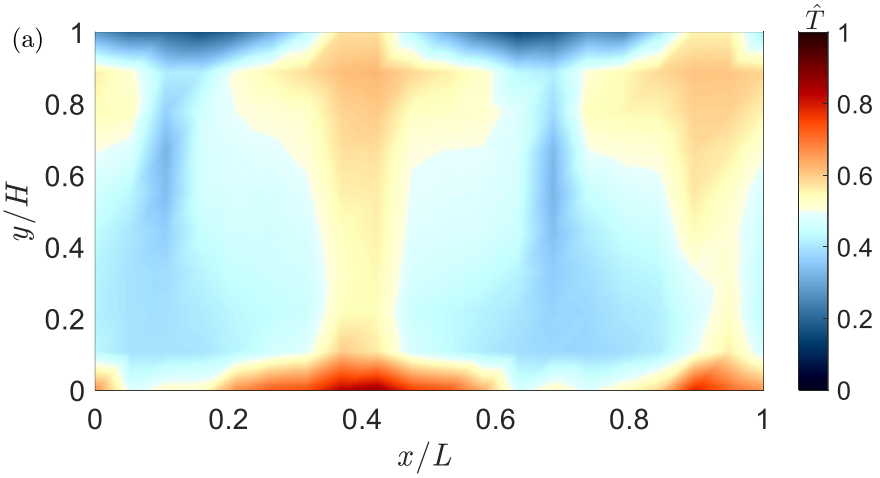

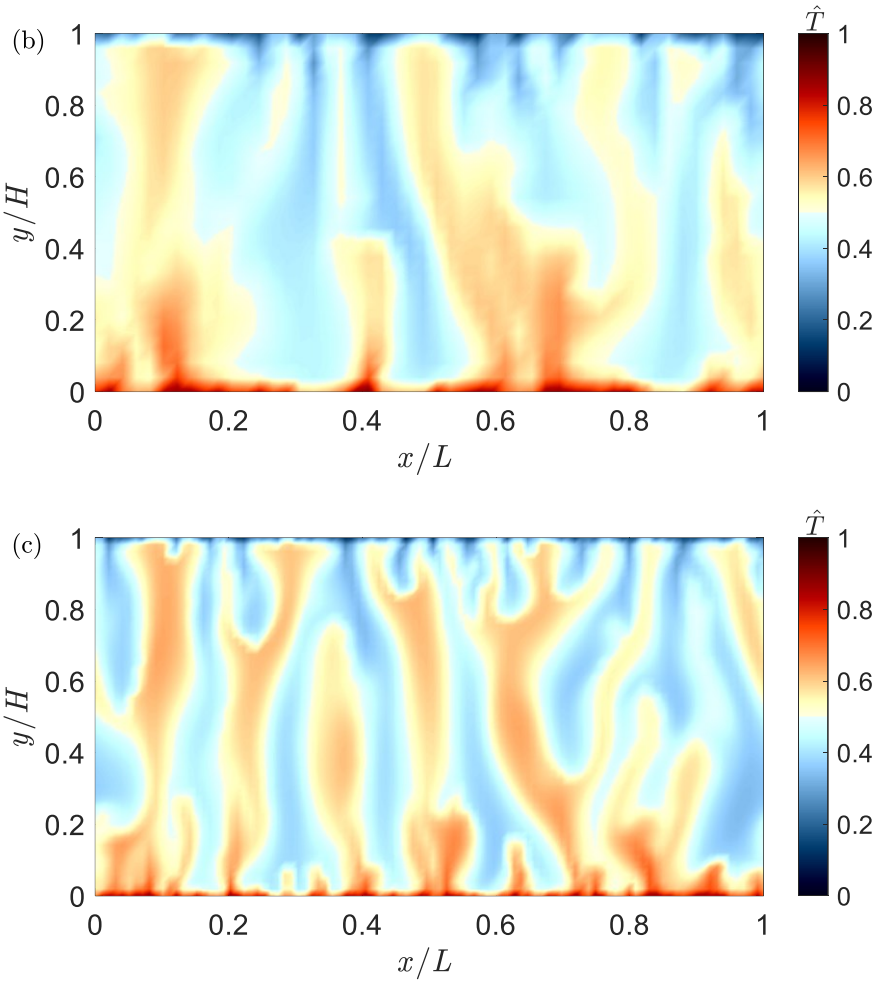

Figure 7: Instantaneous temperature fields at *Ra* = 10 000 from DNS with ϕ = 0.56 for (a) *H*/*m* = 10, (b) *H*/*m* = 25, and (c) *H*/*m* = 50.

To better explain the role of pore size in plume development, the local temperature fields within the first few REVs near the bottom boundary ($y/H = 0$) are plotted in **Figure 8**. With large pore sizes (**Figure 8a**), the flow impedance is reduced and instabilities developed near the boundary layer can interact more easily, giving rise to large structured plume columns. However, at smaller pore sizes (**Figure 8c**), this interaction is largely limited by the solid phase, thus the instabilities at the boundary layers tend to develop into smaller and more frequent plume columns. Again, the DOB results (**Figure 8d**) demonstrate behavior similar to DNS at $H/m = 50$, thus suggesting that DNS and DOB simulations could exhibit the same frequency of mega-plumes as $H/m \rightarrow \infty$. A similar observation was reported by (Gasow *et al.* 2020) when studying mega-plume frequency for solutal convection, thus, it is expected that thermal convection with a highly insulating solid phase would follow this behavior.

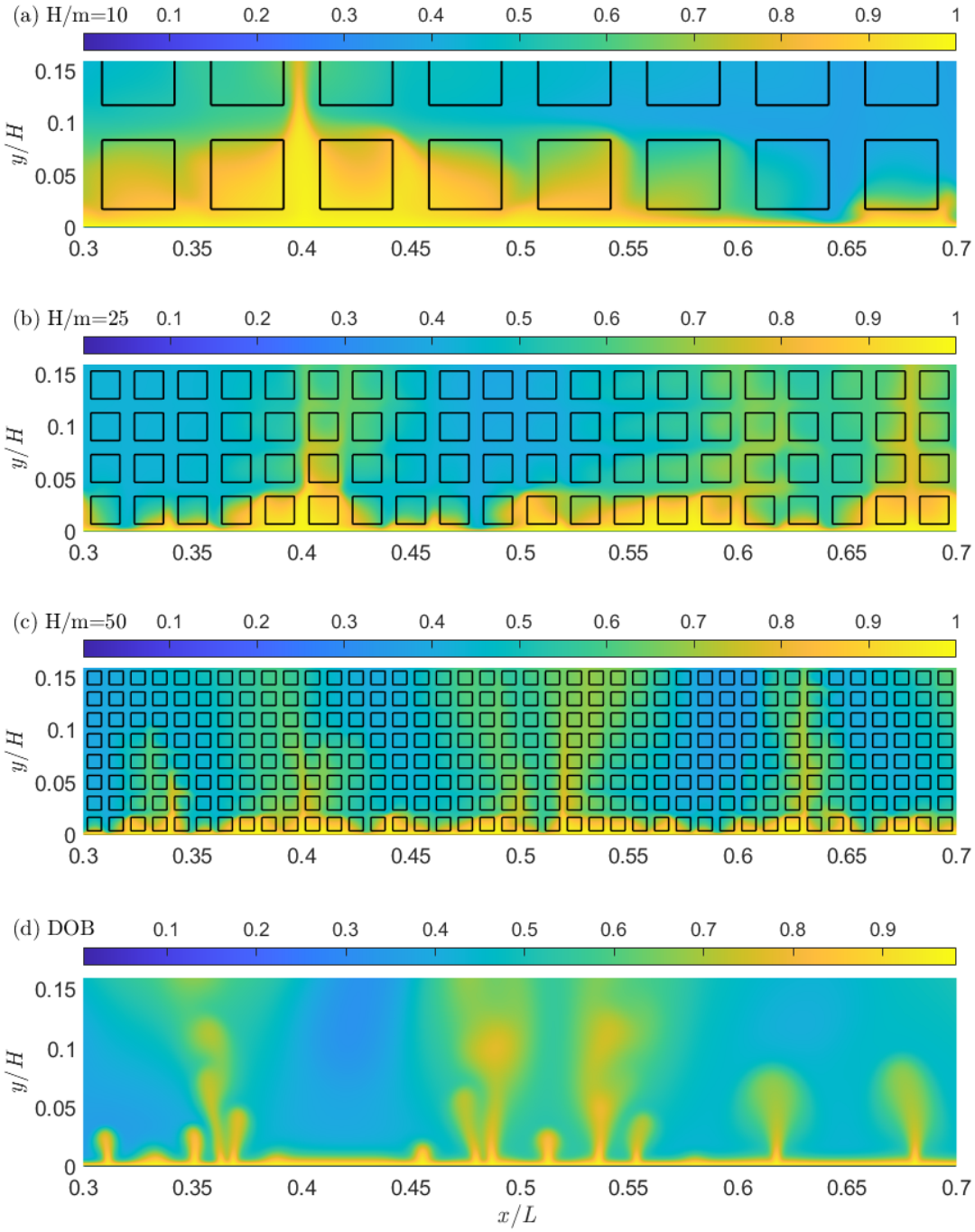

Figure 8: Instantaneous temperature fields near the lower boundary at *Ra* = 10 000 with ϕ = 0.56 from (a) DNS, *H*/*m* = 10, (b) DNS, *H*/*m* = 25, (c) DNS, *H*/*m* = 50, and (d) DOB simulations.

b. Flow structures

To compare the flow structures, we define a local Reynolds number following (Gasow *et al.* 2020) based on the local velocity magnitude:

$$\mathrm{Re}_K = \frac{|\mathbf{u}|\sqrt{K}}{\nu_f} \tag{45}$$

It was noted in (Nield & Bejan 2017) that the Darcy's term dominates the drag for $Re_K << 1$, while the Forchheimer's (quadratic) drag term has greater effects for $Re_K > 1$. The Reynolds number distributions are presented in **Figure 9** for the three REV sizes at Ra = 10 000. The flow structures between three REV sizes are quite distinguishable, where large pores cause a low number of large structured flow paths, while small pore sizes cause numerous chaotic and disordered flow paths. Slightly higher Reynolds numbers are observed for lower H/m. A possible reason for this is the reduction in flow resistance (higher Darcy number at larger pore sizes), however, further study would be required to make a generalized statement of proportionality. Nonetheless, the maximum Reynolds number observed here is ~ 6×10^{-2}, thus we believe that the elimination of the Forchheimer's term is a valid assumption for the ranges of Ra studied.

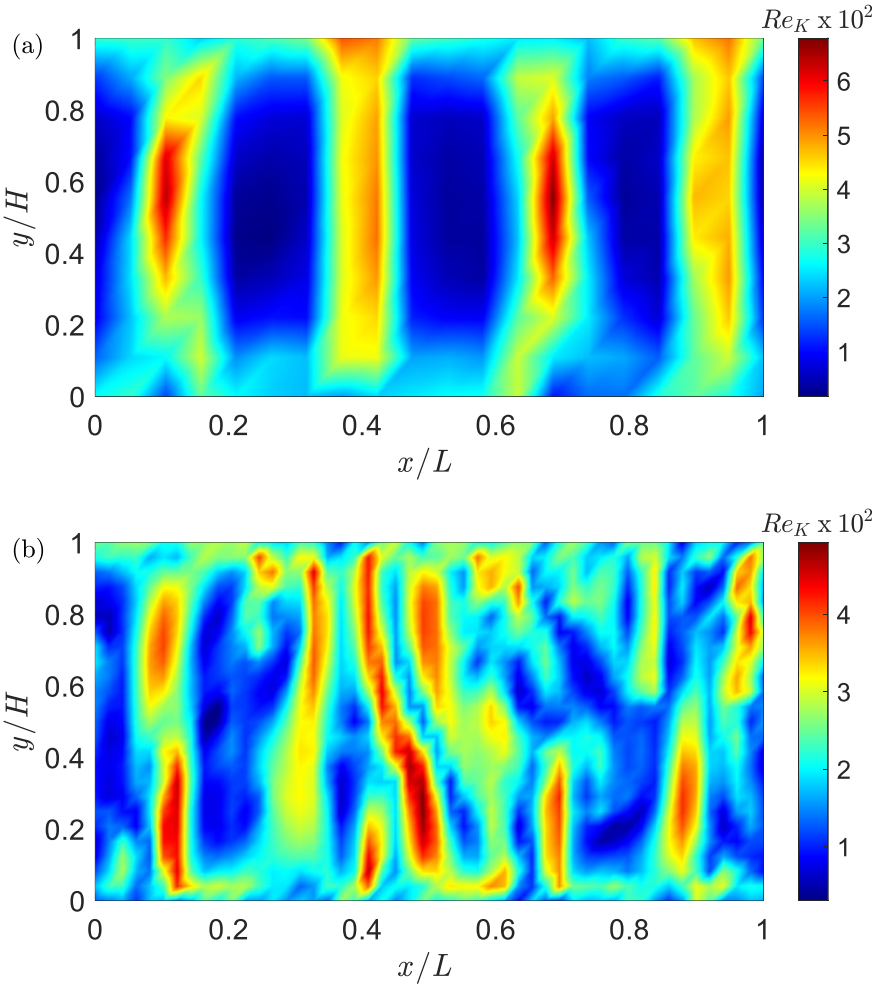

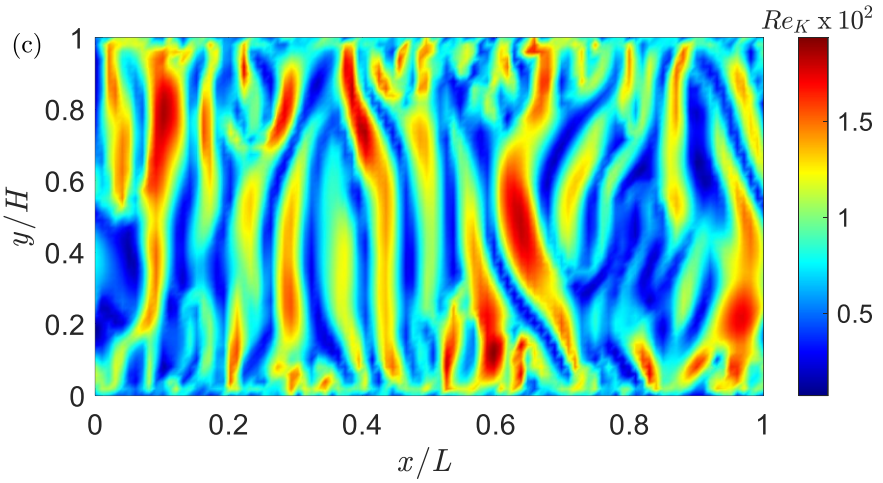

Figure 9: Snapshots of the instantaneous Reynolds number Re_K at Ra=10 000 from DNS with ϕ = 0.56 for (a) H/m = 10, (b) H/m = 25, and (c) H/m = 50.

c. Nu-Ra scaling

Before the discussion on the overall *Nu*-*Ra* scaling, the local *Nu* distributions on the walls at different pores sizes and *Ra* values are examined. **Figure 10** shows the local *Nu* at the bottom boundary for the three pore sizes studied. It is pointed out that the local Nusselt numbers evaluated at the top and bottom walls should exhibit a similar magnitude and frequency of peaks; this was verified in our LBM results across a wide range of parameters, thus the local *Nu* values are only shown at the bottom wall. It is clear from **Figure 10** that at a fixed *Ra* the changes in frequency and magnitude of the local Nusselt number with the pore size follow the trend in plume development shown in **Figure 8**. In addition, the local *Nu* values at the bottom wall from both DNS and DOB models are shown in **Figure 11** for varying *Ra*. While both models show increased number of peaks and overall magnitude in *Nu* when *Ra* increases, the DOB results at *Ra* = 10 000 and 20 000 have considerably more peaks in comparison to DNS. Recalling **Figure 6** and **Figure 7**, DOB simulations exhibit boundary layers filled with quite frequent micro-plumes (also called proto-plumes), however, these micro-plumes appear to be suppressed by the solid phase in DNS, especially at large pore sizes. Thus, a possible explanation for the high frequency *Nu* peaks found in DOB results in **Figure 11** is the inclusion of these micro-plumes, which induce small local changes in the temperature field near and within the boundary layers.

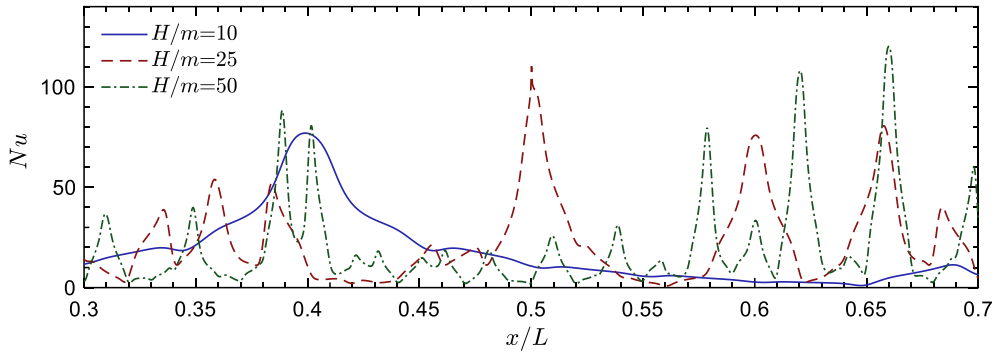

Figure 10: Variation of local Nusselt number with *REV size (H/m)* at bottom wall for *Ra* = 10 000 and ϕ = 0.56.

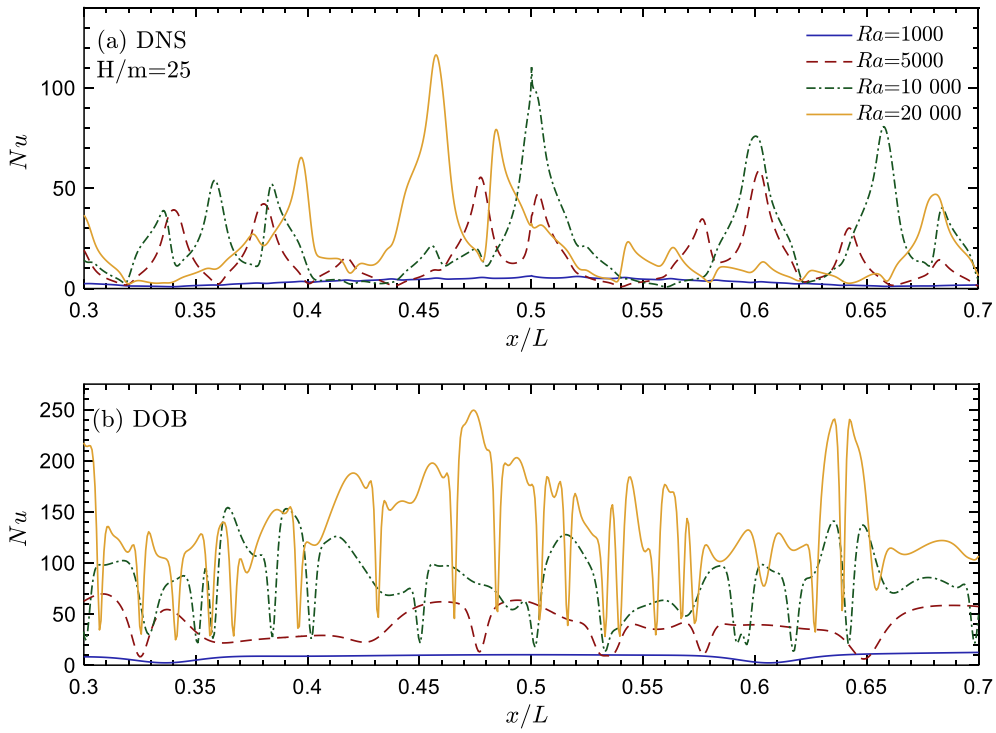

Figure 11: Variation of local Nusselt number with *Ra* at the bottom wall with σ = 1, k_s/k_f = 1, and ϕ = 0.56 from (a) DNS at *H*/*m* = 25 and (b) DOB simulations.

The scaling of the overall Nusselt number for both DOB and DNS results at different pore sizes is given in **Figure 12**. We find that the DOB results overestimate the rate of heat transfer for the range of *Ra* considered here. In contrast to previously computed results for mass transfer (Gasow *et al.* 2020) with no discernible trend in the Sherwood number with pore size, the DNS results shown here suggest that the heat transfer rate increases as pore size decreases. For *H*/*m* = 10, the DNS results appear to trend towards an effective power law near $Nu \propto Ra^{0.319}$ (Keene &

Goldstein 2015) at higher Rayleigh numbers, while for H/m = 50 the scaling remains near $Nu \propto Ra^{0.9}$. Nonetheless, we would expect $Nu \propto Ra^{\sim 0.319}$ scaling to be reached at higher values of Ra regardless of pore size once the length scales of flow become smaller than the pore scale (Hewitt 2020; Liu *et al.* 2020).

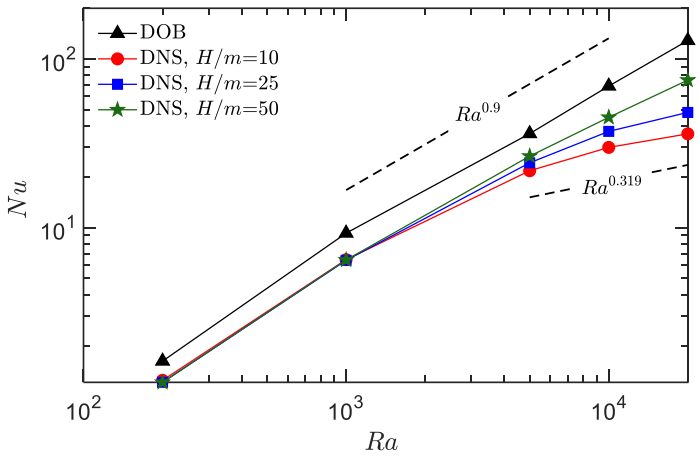

Figure 12: Comparison of *Nu-Ra* relations between DOB and DNS results with different pore sizes and a fixed porosity ϕ = 0.56.

d. Temperature and velocity statistics

First, **Figure 13** shows the vertical profiles of the temporally and horizontally averaged temperature (both scalars and their root mean squares, r.m.s.) and r.m.s. of x- and y-direction velocity components from DOB simulations. It has been suggested (Huppert & Neufeld 2014; Kränzien & Jin 2018) that the boundary layer thickness is determined by $1/Ra$. Thus, we normalize the dimensionless coordinate in **Figure 13** as yRa/H, upon which the temperature and velocity profiles at different Ra become almost identical. This is consistent with the study of pore size effects in mass transfer by Gasow et al. (Gasow *et al.* 2020).

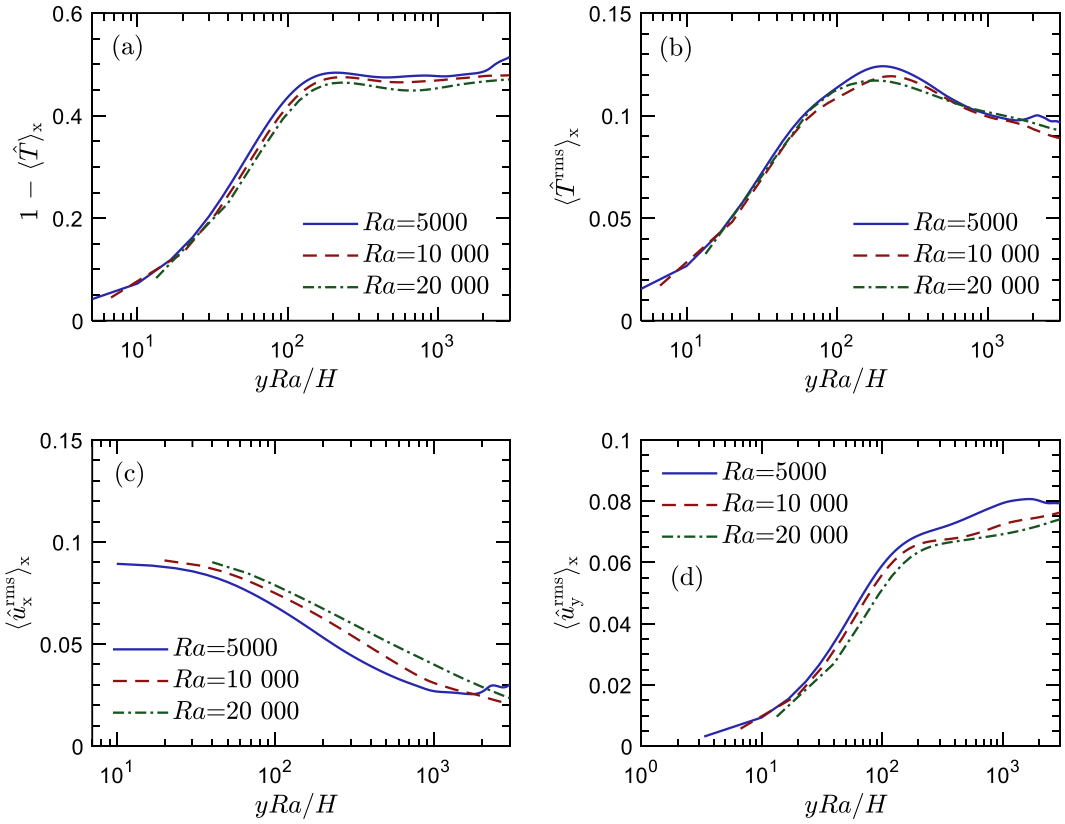

Figure 13: DOB results: (a) vertical profiles of temporally and horizontally averaged temperature, and root mean squares of (b) temperature flunctuation, (c) u_x fluctuation, and (d) u_y fluctuation.

In contrast, normalizing the DNS results at H/m = 25 by yRa/H shows quite different profiles, as shown in **Figure 14**. Gasow et al. suggested that for solutal convection the statistics of the concentration and velocity fields are not only influenced by Ra, but also by the pore size (m/H). We find it instrumental to test the consistency of this observation for thermal convection. Therefore, temporally and horizontally averaged temperature and r.m.s of the temperature and velocity fields at different Rayleigh numbers from DNS are shown in **Figure 15**. We find that the lines collapse when the dimensionless coordinate y/H is scaled by the pore size, suggesting that the pore scale effects play a major role in shaping the boundary layer and flow structure in both thermal and solutal convection. Recent studies have begun to investigate these pore-scale factors for solutal convection through modified/extended DOB equations. Wen et al. (Wen, Chang, & Hesse 2018) investigated the effects of mechanical dispersion through the use of a Fickian dispersion tensor, introducing two additional dimensionless parameters: the dispersive Rayleigh number $Ra_d = H/\varepsilon_t$ and the dispersivity ratio $r = \varepsilon_l/\varepsilon_t$ where ε_t and ε_l are the transverse and

longitudinal dispervities, respectively. Their work showed that increasing the mechanical dispersion would increase the plume spacing, thus showing that the grain/pore size plays a role in shaping the plumes and flow pattern. A recent work by Gasow et al. (Gasow *et al.* 2021) included the effects of momentum dispersion through a "two-length-scale diffusion" model. By considering the pore-scale momentum transport through an effective diffusion term, they were able to obtain more accurate Sherwood numbers than with the traditional DOB equations. Nonetheless, there is still a need to extend and build upon those works for thermal convection where additional phenomena are involved.

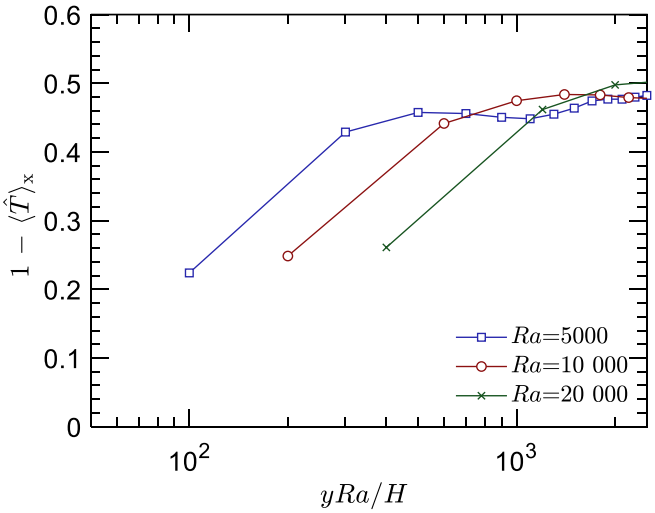

Figure 14: Vertical profiles of temporally and horizontally averaged temperature from DNS at *H*/*m* = 25.

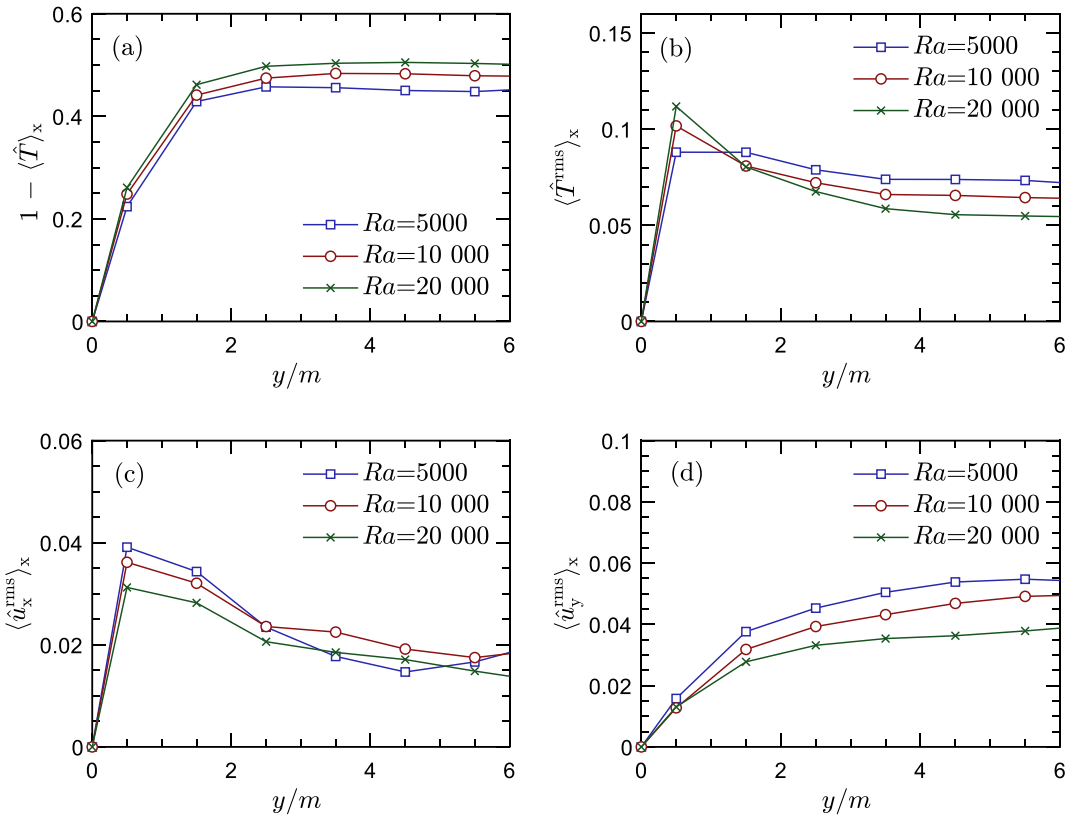

Figure 15: DNS results at *H*/*m* = 25: (a) vertical profiles of temporally and horizontally averaged temperature, and root mean squares of (b) temperature flunctuation, (c) u_x fluctuation, and (d) u_y fluctuation.

C. Effects of conjugate heat transfer

Now we consider the effects of conjugate heat transfer on thermal convection when the fluid and solid phases have different transport properties (e.g., $k_s/k_f \neq 1$ and/or $\sigma \neq 1$). We begin by emphasizing that k_s/k_f and σ are independent parameters with k_s/k_f representing the thermal conductivity ratio and σ the heat capacity ratio, while the thermal diffusivity ratio is related to those two through $\gamma = (k_s/k_f)/\sigma$. To explore the respective effects of both, two groups of cases are examined: (1) Group 1 with varying k_s/k_f at $\sigma = 1$, and (2) Group 2 with varying σ at $k_s/k_f = 1$.

a. Nu-Ra relations

Figure 16 shows the *Nu*-*Ra* relations for various k_s/k_f (Group 1) and ϕ values from both DNS and DOB results. Instantaneous snapshots of the temperature fields at Ra = 20 000 and ϕ = 0.56 can be found in Appendix B. Since the effect of thermal conductivity enters the DOB equations through only Ra and $\overline{\phi} = 1$ when $\sigma = 1$ (see Eq. (17)), a single line is shown for DOB simulations. The DNS results show that both k_s/k_f and porosity ϕ have a significant effect on *Nu*.

A few key observations are noted: (1) at fixed ϕ and Ra, the magnitude of Nu appears to decrease as k_s/k_f increases, (2) for $k_s/k_f < 1$, Nu decreases as ϕ increases; however, for $k_s/k_f > 1$, Nu increases with ϕ, and (3) DOB simulations appear to overpredict the heat transfer rate regardless of k_s/k_f and ϕ, with larger discrepancy observed for higher k_s/k_f and Ra. The effects in points (1) and (2) can be attributed to the physical differences at the pore scale for a fixed Ra. For example, at Ra = 20 000 and ϕ = 0.56 the unconfined Rayleigh number at k_s/k_f = 0.1 is $Ra_f = 1.60 \times 10^9$, while for k_s/k_f = 10 the number is $Ra_f = 8.41 \times 10^9$. Thus, at fixed Ra, ϕ and H/m, Ra_f will be greater for larger k_s/k_f. Furthermore, a larger k_s/k_f is also representative of a more conductive solid phase and varying porosities indicate differences in permeability (higher ϕ yield smaller Ra_f values with fixed Ra, k_s/k_f, and H/m). The major conjecture of the DOB equations is that regardless of k_s/k_f and ϕ, the ratio of the overall to conductive heat transfer rate (i.e., the Nusselt number) is constant across a REV at a fixed Ra. Our DNS results show that this is not true, suggesting that effects of k_s/k_f and ϕ should be considered independently of Ra.

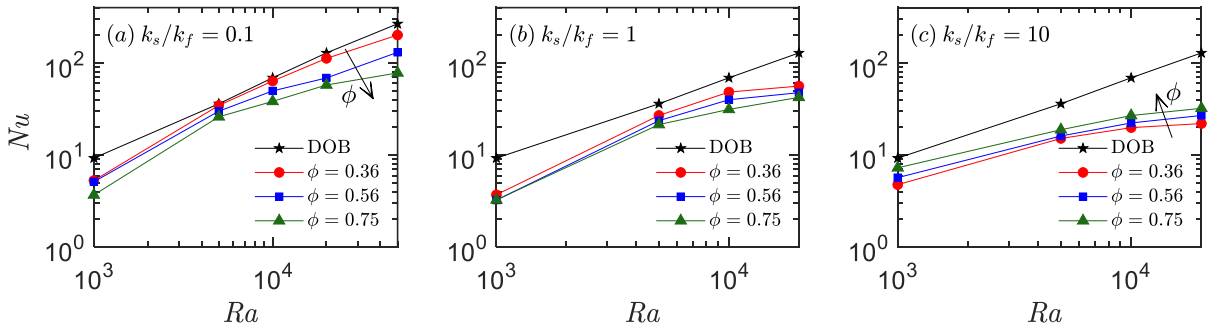

Figure 16: Comparison of *Nu-Ra* relations at different porosities for Group 1 cases (σ = 1): (a) k_s/k_f = 0.1, (b) k_s/k_f = 1, and (c) k_s/k_f = 10. The reference DOB result is independent of both ϕ and k_s/k_f, and H/m = 25 for all DNS results.

As previously mentioned, comparisons of *Nu-Ra* scaling in literature are widespread. Namely, theoretical studies based on the DOB equations have predicted ultimate regime scaling exponents in ranges of 0.9-0.95, while pore-scale and experimental studies have found values closer to 0.29-0.33. Also, the Nu values obtained based on experiments varied largely, raising questions on what parameters (ϕ, H/m, k_s/k_f, etc.) are the main contributors. Previous discussion has shown that both the pore size and k_s/k_f affect the *Nu-Ra* scaling. Thus, we find it valuable to compare selected DNS at varying k_s/k_f and σ to reported experiments (Keene & Goldstein 2015; Kladias & Prasad 1991) as shown in **Figure 17**. The characteristic pore size, H/L_{pore} (L_{pore} is the

pore-scale solid block diameter or width), in experiments ranged from 3.048 to 12.7; while k_s/k_f varied from ~0.33 to ~321. Overall, the DNS results in the limits of k_s/k_f and σ appear to span the range of experimental data reasonably well. The DNS results also capture the nonlinear *Nu-Ra* scaling observed in experiments (Keene & Goldstein 2015).

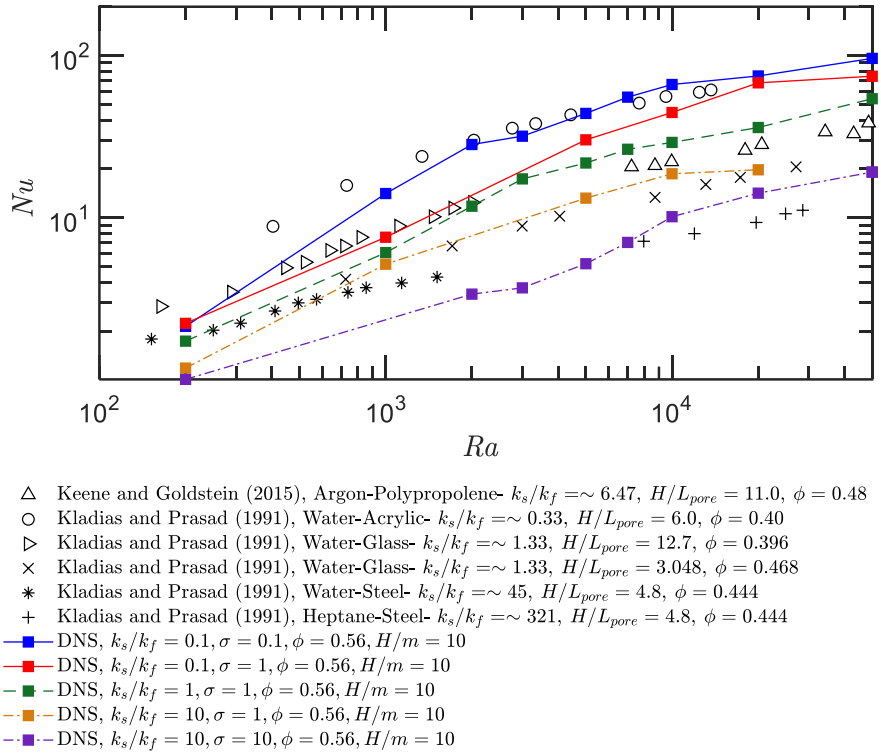

Figure 17: Comparison of *Nu-Ra* relations between reported experiments and present DNS at $H/m = 10$ and $\phi = 0.56$ ($m/d = 1.5$).

Next, we focus on the effects of the heat capacity ratio σ. **Figure 18** presents the *Nu-Ra* relations for $\sigma = 0.1$, 1, and 10 with $k_s/k_f = 1$ fixed (Group 2) from both DOB and DNS results. In contrast to the effect of k_s/k_f, the effects of σ enter the DOB equations through both *Ra* and $\overline{\phi}$ (Eq. 17). In the DOB equations, at a fixed *Ra*, $\overline{\phi}$ is manifested through the convective term $\hat{\nabla}\cdot\left(\hat{\mathbf{u}}\hat{T}/\overline{\phi}\right)$ in Eq. (23). Thus, one would expect the convective strength to follow $1/\overline{\phi}$. This is observed in **Figure 18a-c**, where *Nu* decreases as ϕ increases for $\sigma < 1$ (since $\overline{\phi} = 0.1 + 0.9\phi$ at $\sigma = 0.1$), while *Nu* increases as ϕ increases for $\sigma > 1$ (since $\overline{\phi} = 10 - 9\phi$ at $\sigma = 10$).

Interestingly, the same trend in the variations of *Nu* with σ and ϕ is observed in the DNS results in **Figure 18d-f**, suggesting that the effects of varying σ alter the convection strength in a similar manner in both DOB and DNS results. In the DNS equations, the effects of varying σ at a

fixed Ra are manifested through scaling of Ra_f (also by $1/\bar{\phi}$). Thus, σ plays a similar role in determining the Nusselt number for both DOB and DNS results. In addition, the instantaneous snapshots of the temperature fields for varying σ values from both DOB and DNS results are provided in Appendix B. Both DOB and DNS temperature fields appear to exhibit distinct mega-plume frequency and size, with σ = 0.1 showing more frequent and smaller plumes, and the opposite for σ = 10. This suggests that the peak wavenumber follows $Ra/\bar{\phi}$ for the range of parameters studied here. It should be noted that previous studies have shown that the peak wavenumber is dependent upon the initial fields, aspect ratio of the convection cell, and pore size (Gasow *et al.* 2020; Hewitt *et al.* 2012) and are not unique for $Ra > 39716$ (Wen *et al.* 2015), thus, more detailed investigations are needed to fully characterize the peak wavenumber. This is out of the scope of the present work.

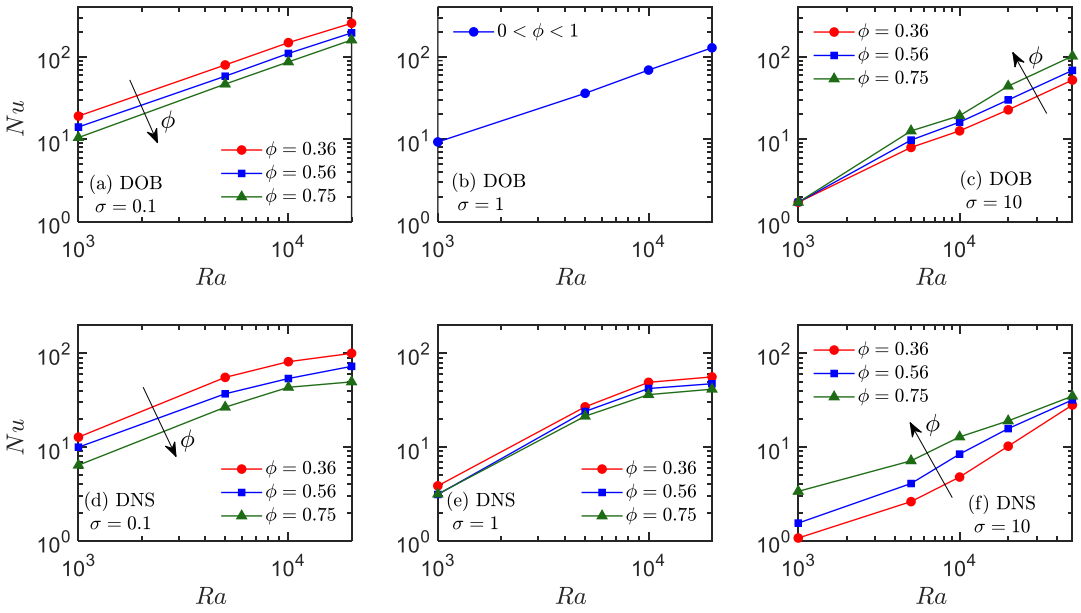

Figure 18: Comparison of *Nu-Ra* relations at different porosities for Group 2 cases (k_s/k_f = 1): (a) σ = 0.1, (b) σ = 1, and (c) σ = 10 are from DOB results, and (d) σ = 0.1, (e) σ = 1, and (f) σ = 10 are from DNS results at H/m = 25.

b. Thermal boundary layer analysis

In this section, we investigate the characteristics of the thermal boundary layers from both DOB and DNS results. As discussed in Section V-B-d, several works based on the DOB equations have suggested that the boundary layer thickness is determined by $1/Ra$ (Gasow *et al.* 2020;

Huppert & Neufeld 2014; Kränzien & Jin 2018), however, these have been limited to cases where $\sigma = 1$. The temporally and horizontally averaged temperature profiles from DOB simulations are first plotted in **Figure 19** when the dimensionless coordinate y/H is scaled by $1/Ra$ following that in **Figure 13a**. It is obvious that in addition to Ra, both ϕ and σ have significant effects on the boundary layer thickness. As the convective term in the DOB equations is scaled by the effective volumetric heat capacity ratio $\overline{\phi}$, we hypothesize that the boundary layer thickness for thermal convection between the two phases with different transport properties be determined by both Ra and $\overline{\phi}$ in the DOB model, and the results are shown in **Figure 20**, where it can be observed that all the temperature profiles effectively collapse to a narrow band, confirming our hypothesis that the thermal boundary layer thickness is determined by $\overline{\phi}/Ra$.

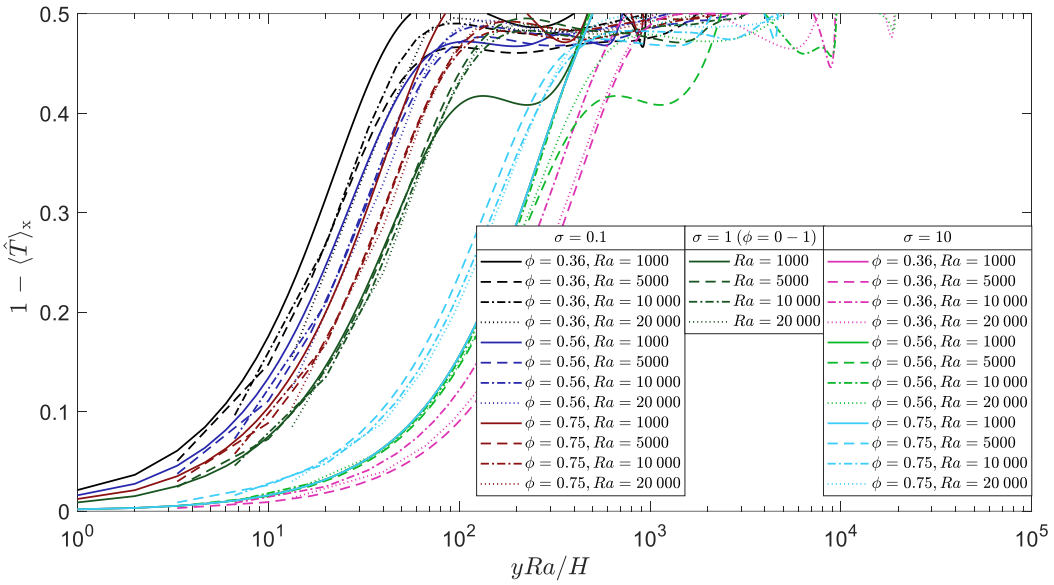

Figure 19: Temporally and horizontally averaged temperature profiles from DOB simulations when y/H is scaled by $1/Ra$.

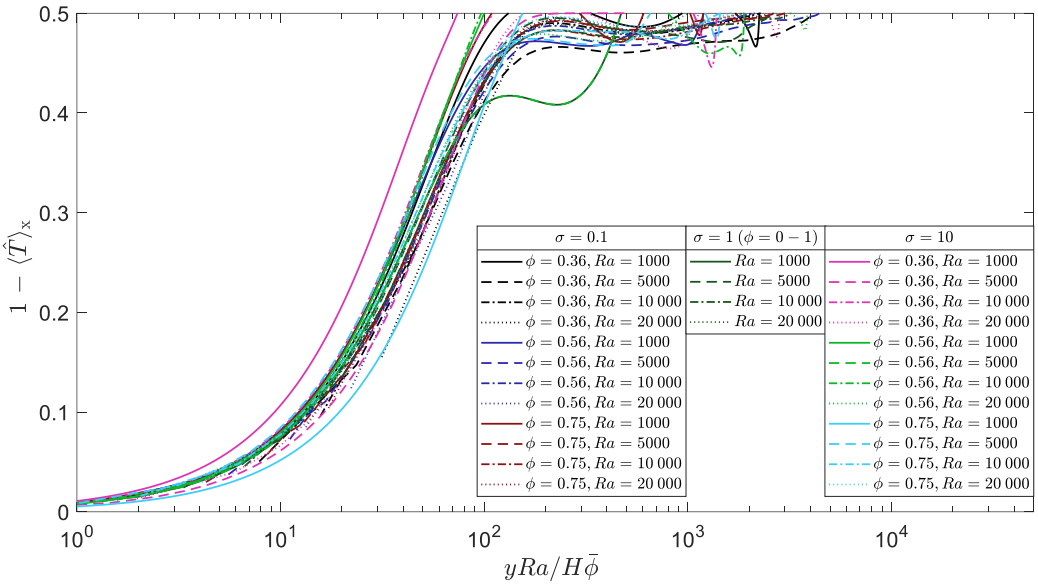

Figure 20: Temporally and horizontally averaged temperature profiles from DOB simulations when *y*/*H* is scaled by $\bar{\phi}/Ra$.

Also as discussed in Section V-B-d, the thermal boundary layer thickness from DNS results at $k_s/k_f = \sigma = 1$ is determined by the pore scale (m/H), consistent with the scaling presented in (Gasow *et al.* 2020) for mass transfer. It is of interest to examine this for $k_s/k_f \neq 1$ and/or $\sigma \neq 1$. **Figure 21** shows results for varying k_s/k_f with $\sigma = 1$ (Group 1) when y/H is rescaled by the pore scale (m/H). Surprisingly, the profiles appear to overlap reasonably well regardless of k_s/k_f and Ra, suggesting that the pore size is also the controlling factor for thermal convection with varying conductivities in the two phases.

We also find it instructive to show in detail the local boundary layers within the first REV. **Figure 22** shows the temperature profiles for $Ra = 10\,000$ and $H/m = 25$ near the lower wall. While the complete boundary layer is determined by the pore size, the local behavior near the boundary is heavily influenced by variations in thermal properties. Near the wall, the boundary layer is encompassed in only the fluid phase, thus we would expect a larger temperature gradient at higher Ra_f (higher k_s/k_f), as noticed in **Figure 22**. Furthermore, the central region of the first REV contains the solid phase. As expected, the temperature gradient in this region is smaller for $k_s/k_f = 10$, and vice versa for $k_s/k_f = 0.1$. This local behavior is altogether uncaptured by the DOB equations, which negate the effects of local temperature and velocity fluctuations captured through thermal

dispersion, $\left(\rho c_p\right)_f \nabla \cdot \left(\phi \left\langle \breve{\mathbf{u}} \breve{\tilde{T}} \right\rangle^f\right)$. The results shown here suggest that future work aimed at improving macroscopic models for thermal convection should consider these local effects.

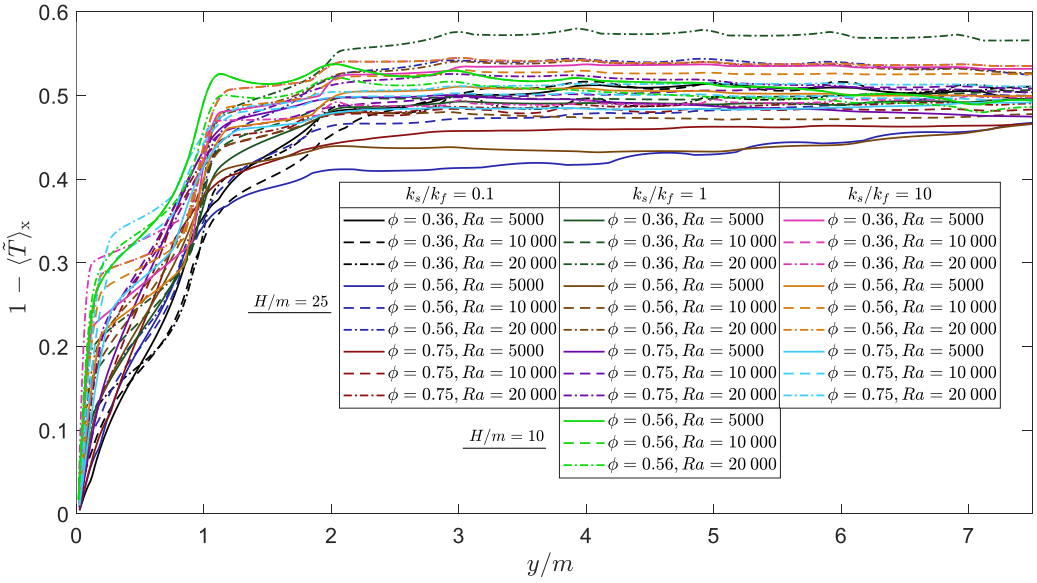

Figure 21: Temporally and horizontally averaged temperature profiles from DNS for Group 1 cases with varying k_s/k_f values when y/H is scaled by m/H.

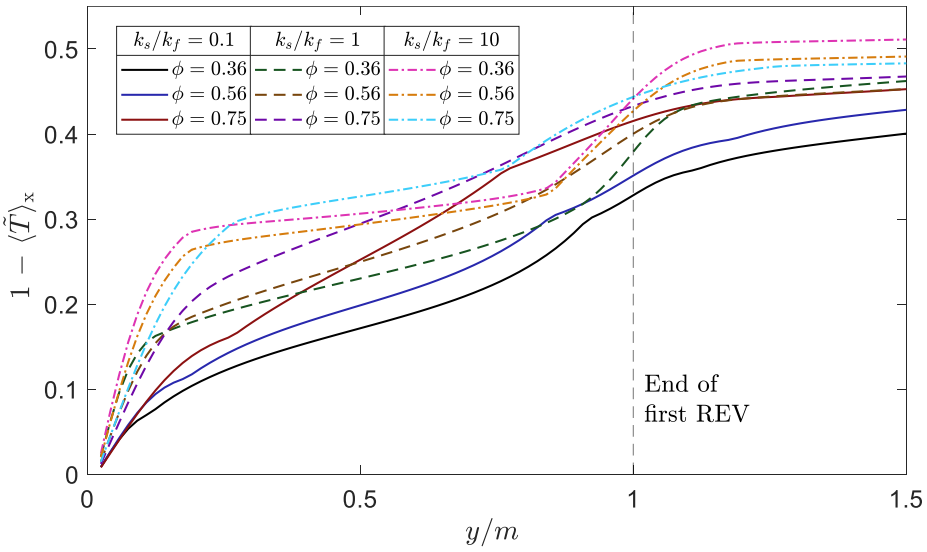

Figure 22: Local temperature profiles from DNS for σ = 1, Ra = 10 000 and H/m = 25.

Furthermore, **Figure 23** shows the results for the varying σ cases with $k_s/k_f = 1$ (Group 2) when y/H is rescaled by the pore size m/H. Similar to Group 1 cases, all profiles at $\sigma = 0.1$ and 1 collapse well. However, for low Ra (~5000) and $\sigma = 10$, the boundary layers are thicker and are

not limited to only the first few REVs, this is again due to the much lower unconfined Rayleigh number Ra_f for those cases. Recalling that Ra_f is related to Ra as $Ra_f = \frac{Ra\left(k_m/k_f\right)}{Da\left[\phi+\left(1-\phi\right)\sigma\right]}$, larger σ values indicate smaller Ra_f, for which the convection will be less significant and conduction can become dominant (e.g., when $\sigma \to \infty$, $Ra_f \to 0$ and pure conduction is attained). The profiles at Ra = 5000 and σ = 10 demonstrate the onset of this behavior. Overall, the present boundary layer analysis between the DOB and DNS results clearly demonstrates the distinct local behaviors that would contribute to the different thermal convection characteristics in porous media when formulated through the DNS and the volume-averaged DOB equations with additional assumptions.

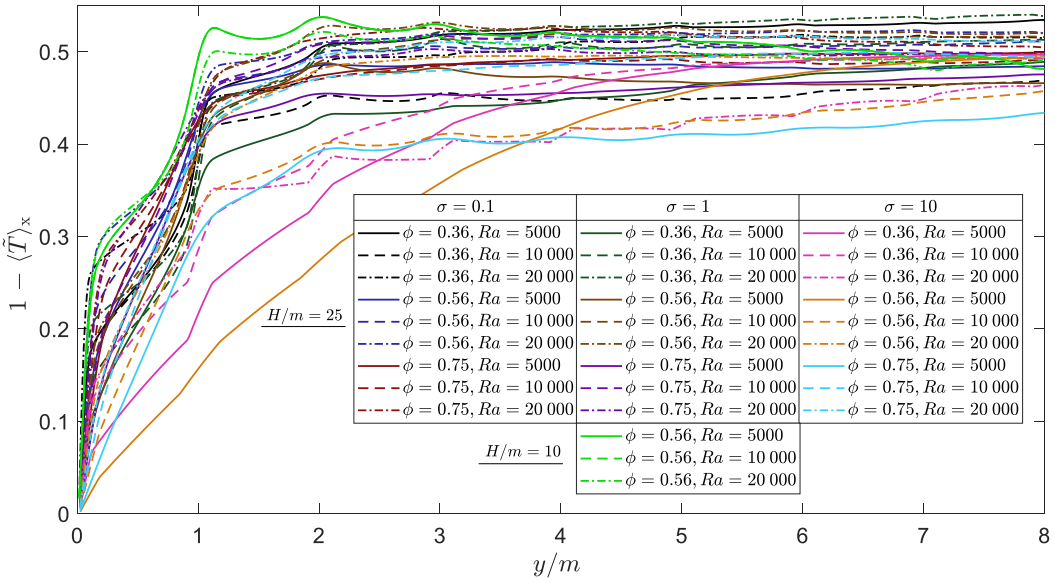

Figure 23: Temporally and horizontally averaged temperature profiles from DNS for Group 2 cases with varying σ values when y/H *is* scaled by m/H.

VI. Conclusions

We performed high resolution DNS of thermal convection in a simplified 2D porous structure and compared results to volume-averaged formulations based on the DOB equations. Both DNS and DOB simulations were realized with the LBM, with a novel method of solving the SFM equations with the LBM being proposed and validated. Comparisons of DNS and DOB

results demonstrated that both the pore size and conjugate heat transfer play large roles in shaping the structure of the thermal and flow fields and in determining the Nusselt number.

Upon comparing different pore sizes from DNS, it was found that larger pores (higher Darcy number) created less frequent but structured plumes, and the opposite for smaller pores. Between DNS and DOB results, the temperature fields matched quite well for small pores with $H/m = 50$. A possible explanation for this is that the terms considered in the DOB equation (on the order of $1/Da$) dominate in the interior regime, while the boundary layer is governed instead by the pore size within the first few REVs. The flow structure was compared for all REV sizes at $Ra = 10\,000$. Results showed that the local Reynolds number increased with pore size, however, it is stressed that a detailed analysis of the effects of porosity and the Rayleigh number would be required to make a generalized statement and is considered out of the scope of this paper. We believe the elimination of the Forchheimer term in the DOB equations is valid for the range of Ra studied, as evidenced by the low magnitudes of Re_K (near 7×10^{-2} at $Ra = 10\,000$).

On the effects of conjugate heat transfer, we studied two groups of cases: Group 1 with varying k_s/k_f at $\sigma = 1$, and Group 2 with varying σ at $k_s/k_f = 1$. When comparing the Nusselt numbers for different k_s/k_f and ϕ at fixed Ra (Group 1), we observed that the DNS results predict a decrease in Nu with increasing ϕ when $k_s/k_f < 1$, and the opposite for $k_s/k_f > 1$. This behavior was altogether uncaptured by the DOB equations that only account for the conductivity ratio through Ra. For varying σ (Group 2), a similar trend was observed in both DOB and DNS results, i.e., Nu decreases as ϕ increases for $\sigma < 1$, and the opposite for $\sigma > 1$. This is attributed to the scaling of the convective term in the DOB equations and scaling of Ra_f in the DNS equations. Furthermore, a comparison of $Nu = f(Ra)$ scaling with selected experiments of thermal convection was shown. DNS results demonstrated large variations in Nu for different k_s/k_f and σ and appeared to approach power law scaling near $Nu \propto Ra^{\sim 0.319}$ at high Ra. In comparison, the DOB model maintains scaling of $Nu \propto Ra^{0.9}$. The variations in pore size and thermal conductivity ratio observed in DNS help to explain the large scatter of $Nu = f(Ra)$ data in the literature for thermal convection.

A detailed analysis of the temporally and horizontally averaged temperature profiles was also performed for both DOB and DNS results. Following previous works based on the DOB equations that suggest $1/Ra$ scaling, a unified extended scaling was proposed as $\bar{\phi}/Ra$ to account for the effects of different transport properties. When the dimensionless coordinate y/H is rescaled by $\bar{\phi}/Ra$, the temperature profiles in the boundary layer were shown to collapse for a wide range

of inputs (Ra = 1000 to 20 000 at different ϕ and σ values). Furthermore, the boundary layer thickness from DNS results is determined by the pore size (m/H) for general cases, which is consistent with recent works on mass convection (Gasow *et al.* 2020, 2021). For the special cases at low Ra and high σ in Group 2, the boundary layers were thicker due to the decrease in convection strength (Ra_f is considerably smaller for these cases).

Overall, our results presented herein show that conjugate heat transfer and pore-scale parameters play essential roles in the dynamics of thermal convection. While the DOB equations are useful for situations where it is impractical to obtain/simulate the porous domain, care should be taken to verify that L_{pore}/H is sufficiently small for the volume-averaging to be applied and that the thermal properties are reasonably close. Furthermore, our results along with previously reported observations of mass transfer allow for possible improvement of the DOB models, where underlying physics including pore-scale parameters and boundary layer behavior can be included through the addition of momentum dispersion, thermal dispersion, and viscous diffusion terms.

Acknowledgements

The authors gratefully acknowledge the support of the National Science Foundation, United States (NSF award number OIA 2031701). The computer simulations used the NSF Extreme Science and Engineering Discovery Environment (XSEDE) under award allocation number TG-DMR190112 and the clusters in the High Performance Computing Collaboratory (HPC^2) at Mississippi State University. The authors also thank the three anonymous reviewers for their valuable comments that helped improve this paper.

Declaration of interests

The authors report no conflict of interest.

Supplementary materials

Videos of temperature evolution for DOB simulations performed at k_s/k_f = 1and σ = 1 can be found at:

Movie 1: Temperature evolution for DOB simulation at Ra = 5000
Movie 2: Temperature evolution for DOB simulation at Ra = 10 000
Movie 3: Temperature evolution for DOB simulation at Ra = 20 000

Videos of temperature evolution for DNS performed at k_s/k_f = 1, σ = 1, H/m = 25, and ϕ = 0.56 can be found at:

Movie 4: Temperature evolution for DNS at Ra = 5000
Movie 5: Temperature evolution for DNS at Ra = 10 000
Movie 6: Temperature evolution for DNS at Ra = 20 000

Appendix A. Model validation to solutal convection

In this Appendix, we provide additional comparisons and details used for model validation. Following the discussion in section IV-A, instantaneous contours of the concentration field at Ra = 20 000, H/m = 20, and m/d = 1.5 from the DNS and DOB models are given in **Figure A-1** and **Figure A-2**, respectively. The shape of the mega-plumes and micro-plumic development near the boundary layers are quantitively compared to Figure 4b and Figure 4c in (Gasow *et al.* 2020), demonstrating good agreement.

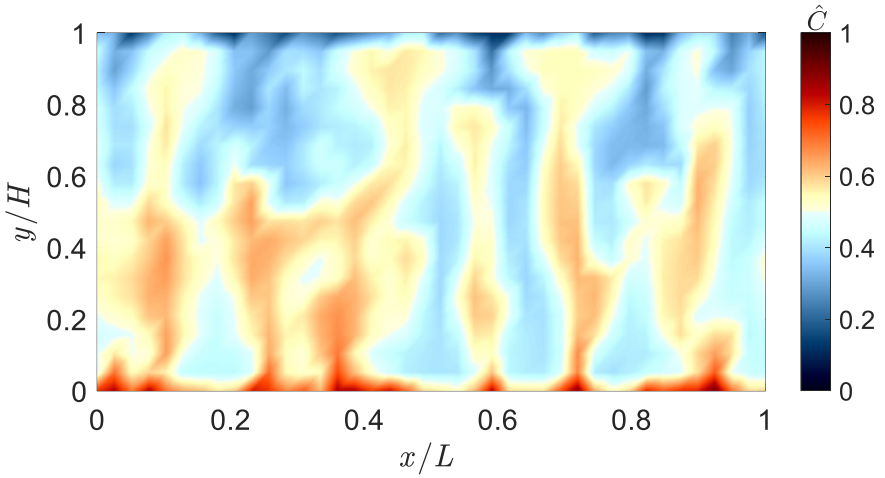

Figure A-1: DNS based instantaneous concentration field for *Ra* = 20 000, *H*/*m* = 20, and *m*/*d* = 1.5 (comparable to Figure 4b in (Gasow *et al.* 2020)**).**

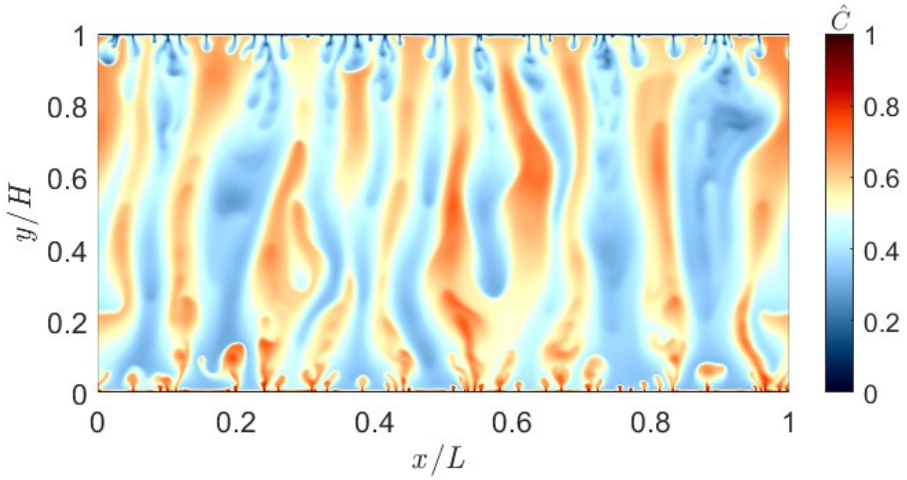

Figure A-2: DOB based instantaneous concentration field for *Ra* = 20 000 (comparable to Figure 4c in (Gasow *et al.* 2020)**).**

Appendix B. Additional temperature contours for *Ra* = 20 000 from DNS and DOB models

Following the discussion in Section V-C-a, instantaneous temperature contours from the DOB model at $Ra = 20\,000$ and $\phi = 0.56$ with varying σ are provided in **Figure B-1**. A clear distinction in the size and frequency of the mega-plumes is present. **Figure B-2** gives the instantaneous temperature contours from DNS at $Ra = 20\,000$, $k_s/k_f = \sigma = 1$, $\phi = 0.56$ and $H/m = 25$, while **Figure B-3** and **Figure B-4** give the corresponding results at varying k_s/k_f cases with $\sigma = 1$ (Group 1) and varying σ with $k_s/k_f = 1$ (Group 2), respectively.

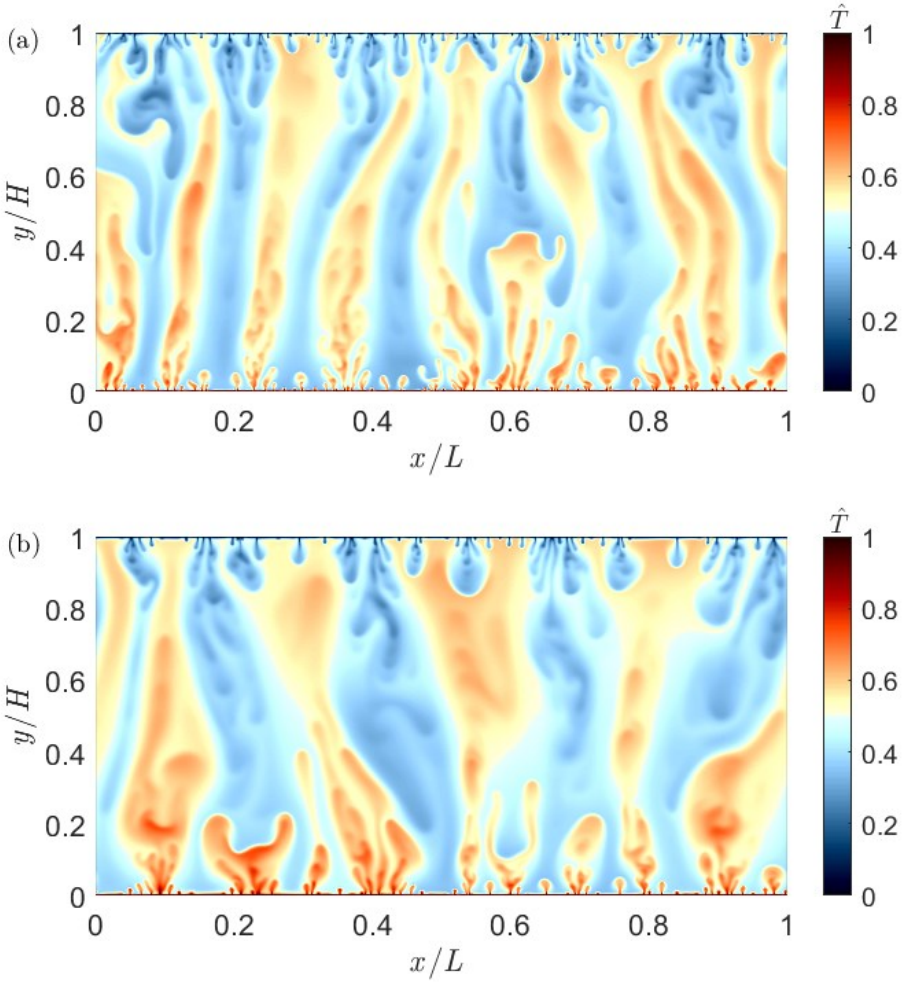

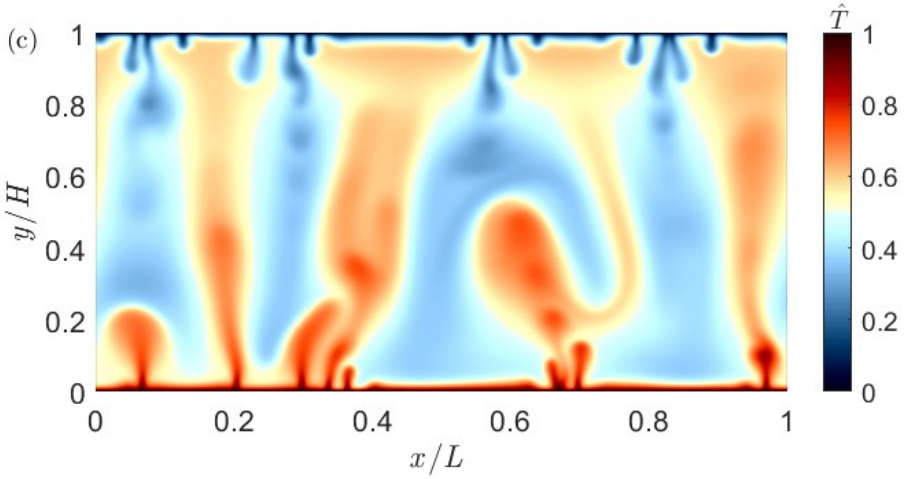

Figure B-1: Instantaneous temperature fields at *Ra*=20 000 and (a) σ = 0.1, (b) σ = 1, and (c) σ = 10 from DOB simulations.

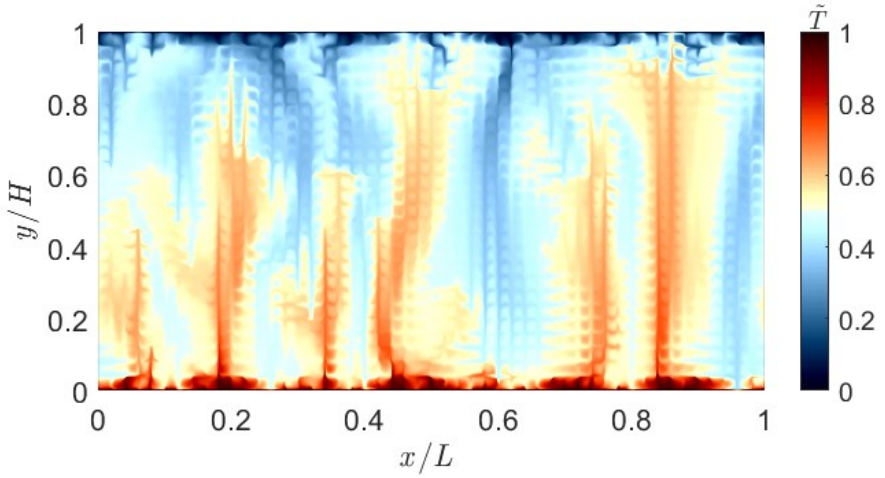

Figure B-2: Instantaneous temperature fields at *Ra* = 20 000, k_s/k_f = σ = 1, ϕ = 0.56, and *H*/*m* = 25 from DNS.

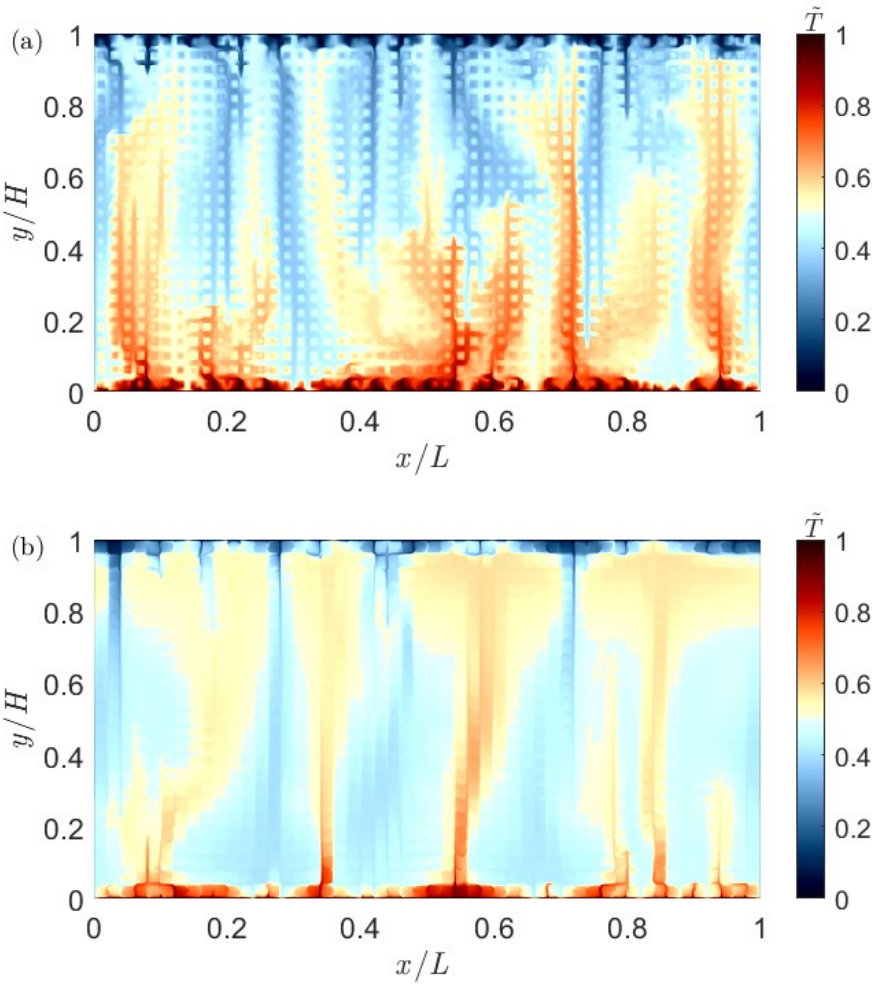

Figure B-3: Instantaneous temperature fields at Ra = 20 000, σ = 1, ϕ = 0.56, H/m = 25, and (a) k_s/k_f = 0.1 and (b) k_s/k_f = 10 from DNS.

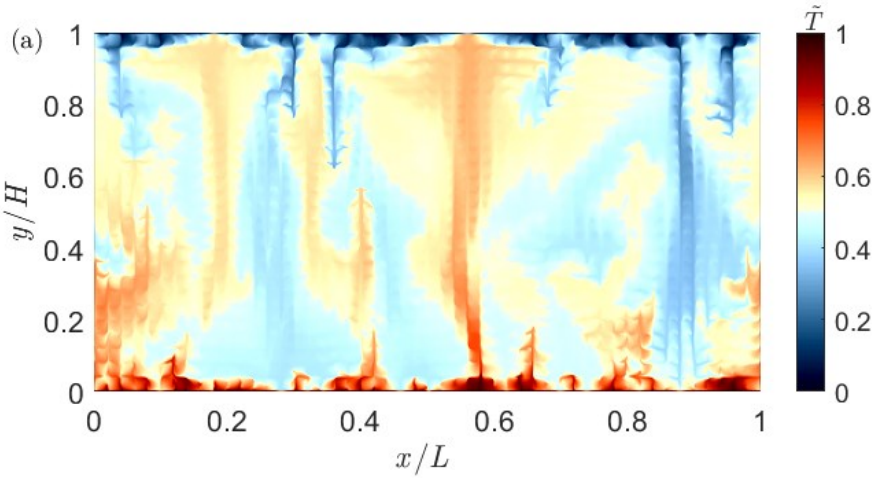

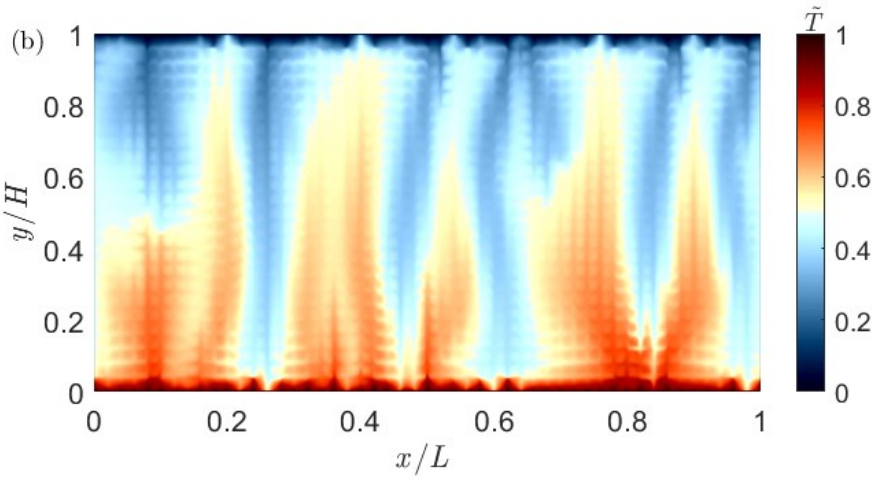

Figure B-4: Instantaneous temperature fields at Ra = 20 000, k_s/k_f = 1, ϕ = 0.56, H/m = 25, and (a) σ = 0.1 and (b) σ = 10 from DNS.

References

Ahlers, G., Grossmann, S., & Lohse, D. (2009). Heat transfer and large scale dynamics in turbulent Rayleigh-Bénard convection. *Reviews of Modern Physics*, **81**(2), 503–537.

Aidun, C. K., & Clausen, J. R. (2010). Lattice-boltzmann method for complex flows. *Annual Review of Fluid Mechanics*, **42**, 439–472.

Benzi, R., Succi, S., & Vergassola, M. (1992). The lattice Boltzmann equation: theory and applications. *Physics Reports*, **222**(3), 145–197.

Chen, S., & Doolen, G. D. (1998). Lattice Boltzmann Method. *Annual Review of Fluid Mechanics*, **30**, 329–364.

Chillà, F., & Schumacher, J. (2012). New perspectives in turbulent Rayleigh-Bénard convection. *European Physical Journal E*, **35**(7). doi:10.1140/epje/i2012-12058-1

Cinar, Y., Riaz, A., & Tchelepi, H. A. (2009). Experimental study of CO2 injection into saline formations. *SPE Journal*, **14**(4), 588–594.

Davidson, J. H., Kulacki, F. A., & Savela, D. (2009). Natural convection in water-saturated reticulated vitreous carbon foam. *International Journal of Heat and Mass Transfer*, **52**, 4479–4483.

de Lemos, M. J. S. (2012). *Turbulence in Porous Media: Modeling and Applications*, 2nd edn.

De Paoli, M., Zonta, F., & Soldati, A. (2016). Influence of anisotropic permeability on convection in porous media: Implications for geological Co2 sequestration. *Physics of Fluids*, **28**(5). doi:10.1063/1.4947425

Gasow, S., Kuznetsov, A. V., Avila, M., & Jin, Y. (2021). A macroscopic two-length-scale model for natural convection in porous media driven by a species-concentration gradient. *Journal of Fluid Mechanics*, **926**. doi:10.1017/jfm.2021.691

Gasow, S., Lin, Z., Zhang, H. C., Kuznetsov, A. V., Avila, M., & Jin, Y. (2020). Effects of pore scale on the macroscopic properties of natural convection in porous media. *Journal of Fluid Mechanics*, **891**(A25), 1–22.

Gasparini, P., & Mantovani, M. S. M. (1984). Heat Transfer in Geothermal Areas., **14**, 9–39.

Hassanzadeh, H., Pooladi-Darvish, M., & Keith, D. (2012). Scaling Behavior of Convective Mixing, with Application to Geological Storage of CO2. *AIChE Journal*, **53**(5), 1121–1131.

He, X., Funfschilling, D., Bodenschatz, E., & Ahlers, G. (2012a). Heat transport by turbulent Rayleigh-Bénard convection for Pr ≃ 0.8 and 4×10 11 ≲ Ra ≲ 2×10 14: Ultimate-state transition for aspect ratio Γ = 1.00. *New Journal of Physics*, **14**. doi:10.1088/1367-2630/14/6/063030

He, X., Funfschilling, D., Nobach, H., Bodenschatz, E., & Ahlers, G. (2012b). Transition to the ultimate state of turbulent rayleigh-bénard convection. *Physical Review Letters*, **108**(2), 1–5.

He, X., & Luo, L.-S. (1997). Lattice Boltzmann Model for the Incompressible Navier-Stokes Equation. *Journal of Statistical Physics*, **88**(3/4), 927–944.

Hewitt, D. R. (2020). Vigorous convection in porous media. *Proceedings of the Royal Society A*, **476**(2239), 1–34.

Hewitt, D. R., Neufeld, J. A., & Lister, J. R. (2012). Ultimate Regime of High Rayleigh Number Convection in a Porous Medium. *Physical Review Letters*, **108**(224503), 1–4.

Hewitt, D. R., Neufeld, J. A., & Lister, J. R. (2013). Convective shutdown in a porous medium at high Rayleigh number. *Journal of Fluid Mechanics*, **719**, 551–586.

Hewitt, D. R., Neufeld, J. A., & Lister, J. R. (2014). High Rayleigh number convection in a three-dimensional porous medium. *Journal of Fluid Mechanics*, **748**, 879–895.

Huppert, H. E., & Neufeld, J. A. (2014). The fluid mechanics of carbon dioxide sequestration. *Annual Review of Fluid Mechanics*, **46**, 255–272.

Iyer, K. P., Scheel, J. D., Schumacher, J., & Sreenivasan, K. R. (2020). Classical 1/3 scaling of convection holds up to Ra = 1015. *Proceedings of the National Academy of Sciences of the United States of America*, **117**(14), 7594–7598.

Jonsson, T., & Catton, I. (1985). Prandtl Number Dependence of Natural Convection in Porous Medium. *American Society of Mechanical Engineers, Heat Transfer Division, (Publication) HTD*, **46**(May 1987), 21–29.

Karani, H., & Huber, C. (2017). Role of thermal disequilibrium on natural convection in porous media: Insights from pore-scale study. *Physical Review E*, **95**(033123), 1–12.

Karani, H., Rashtbehesht, M., Huber, C., & Magin, R. L. (2017). Onset of fractional-order thermal convection in porous media. *Physical Review E*, **96**, 1–8.

Keene, D. J., & Goldstein, R. J. (2015). Thermal convection in porous media at high Rayleigh numbers. *American Society of Mechanical Engineers, Heat Transfer Division, (Publication) HTD*, **137**(3), 1–4.

Kladias, N., & Prasad, V. (1991). Experimental verification of darcy-Brinkman-Forchheimer flow model for natural convection in porous media. *Journal of Thermophysics and Heat Transfer*, **5**(4), 560–576.

Korba, D., Wang, N., & Li, L. (2020). Accuracy of interface schemes for conjugate heat and mass transfer in the lattice Boltzmann method. *International Journal of Heat and Mass Transfer*, **156**, 119694.

Kränzien, P. U., & Jin, Y. (2018). Natural Convection in a Two-Dimensional Cell Filled with a Porous Medium : A Direct Numerical Simulation Study. *Heat Transfer Engineering*, **0**(0), 1–10.

Lallemand, P., & Luo, L.-S. (2000). Theory of the lattice Boltzmann method: Dispersion, dissipation, isotropy, Galilean invariance, and stability. *Physical Review E*, **61**(6), 6546–6562.

Le Reun, T., & Hewitt, D. R. (2021). High-Rayleigh-number convection in porous-fluid layers. *Journal of Fluid Mechanics*, **920**, 1–26.

Li, L., Chen, C., Mei, R., & Klausner, J. F. (2014). Conjugate heat and mass transfer in the lattice Boltzmann equation method. *Physical Review E - Statistical, Nonlinear, and Soft Matter Physics*. doi:10.1103/PhysRevE.89.043308

Li, L., Mei, R., & Klausner, J. F. (2013). Boundary conditions for thermal lattice Boltzmann equation method. *Journal of Computational Physics*, **237**, 366–395.

Li, L., Mei, R., & Klausner, J. F. (2017). Lattice Boltzmann models for the convection-diffusion equation: D2Q5 vs D2Q9. *International Journal of Heat and Mass Transfer*, **108**, 41–62.

Li, X., He, J., Tian, Y., Hao, P., & Huang, S. (2021). Effects of Prandtl number in quasi- two-dimensional Rayleigh – Bénard convection. *Journal of Fluid Mechanics*, **915**(A60), 1–23.

Liang, Y., Wen, B., Hesse, M. A., & DiCarlo, D. (2018). Effect of Dispersion on Solutal Convection in Porous Media. *Geophysical Research Letters*, **45**(18), 9690–9698.

Lister, C. R. B. (1990). An explanation for the multivalued heat transport found experimentally for convection in a porous medium. *Journal of Fluid Mechanics*, **214**(6), 287–320.

Liu, S., Jiang, L., Chong, K. L., & Zhu, X. (2020). From Rayleigh – Bénard convection to porous-media convection : how porosity affects heat transfer and flow structure. *Journal of Fluid Mechanics*, **895**(A18), 1–25.

Lohse, D., & Xia, K. Q. (2010). Small-scale properties of turbulent rayleigh-benard convection. *Annual Review of Fluid Mechanics*, **42**, 335–364.

Luo, L.-S. (1993). Lattice-gas automata and lattice Boltzmann equations for two-dimensional hydrodynamics. *Ph.D. Thesis, Georgia Institute of Technology*, 274.

Miansari, M., Gorji, M., Ganji, D. D., & Hooman, K. (2015). Comparison between continuum and porous continuum models in studying natural convection in porous cavity with random distribution of solid obstacles. *International Journal of Numerical Methods for Heat and Fluid Flow*, **25**(3), 484–503.

Nield, D. A., & Bejan, A. (2017). *Convection in Porous Media*, Fifth, Springer International Publishing AG. doi:10.1007/978-3-319-49562-0

Niemela, J. J., Skrbek, L., Sreenivasan, K. S., & Donnelly, R. J. (2000). Turbulent convection in very high Rayleigh numbers. *Nature*, **404**(April), 837–840.

Otero, J., Dontcheva, L. A., Johnston, H., … Doering, C. R. (2004). High-Rayleigh-number convection in a fluid-saturated porous layer. *Journal of Fluid Mechanics*, **500**, 263–281.

Poel, P. van der P., Stevens, R. J. A. M., & Lohse, D. (2013). Comparison between two- and three-dimensional Rayleigh–Bénard convection. *Journal of Fluid Mechanics*, **736**, 177–194.

Qiang, W., Xie, M., Liu, Z., Wang, Y., Cao, H., & Zhou, H. (2021). Asymptotic behaviour of heat transfer in two-dimensional turbulent convection with high-porosity fluid-saturated media. *Journal of Fluid Mechanics*, **923**, 1–24.

Ratouis, T. M. P., & Zarrouk, S. J. (2016). Factors controlling large-scale hydrodynamic convection in the Taupo Volcanic Zone (TVZ), New Zealand. *Geothermics*, **59**, 236–251.

Roche, P., Castaing, B., Chabaud, B., & Hebral, B. (2001). Observation of the 1 power law in Rayleigh-Be´nard convection. *Physical Review E*, **63**(045303), 1–4.

Shishkina, O., Jam Stevens, R., Grossmann, S., & Lohse, D. (2010). Boundary layer structure in turbulent thermal convection and its consequences for the required numerical resolution. *New Journal of Physics*, **12**(075022). doi:10.1088/1367-2630/12/7/075022

Siggia, E. (1994). High rayleigh number convection. *Annual Review of Fluid Mechanics*, **26**, 137–168.

Toppaladoddi, S., Succi, S., & Wettlaufer, J. S. (2017). Roughness as a Route to the Ultimate Regime of Thermal Convection. *Physical Review Letters*, **118**(7), 1–5.

Tummers, M. J., & Steunebrink, M. (2019). Effect of surface roughness on heat transfer in Rayleigh-Bénard convection. *International Journal of Heat and Mass Transfer*, **139**, 1056–1064.

Wang, M., & Pan, N. (2008). Predictions of effective physical properties of complex multiphase materials. *Materials Science and Engineering R: Reports*, **63**(1), 1–30.

Wen, B., Chang, K. W., & Hesse, M. A. (2018). Rayleigh-Darcy convection with hydrodynamic dispersion. *Physical Review Fluids*, **3**(12), 1–18.

Wen, B., Corson, L. T., & Chini, G. P. (2015). Structure and stability of steady porous medium convection at large Rayleigh number. *Journal of Fluid Mechanics*, **772**, 197–224.

Wilson, A., & Ruppel, C. (2007). Salt tectonics and shallow subseafloor fluid convection: Models of coupled fluid-heat-salt transport. *Geofluids*, **7**(4), 377–386.

Yoshida, H., & Nagaoka, M. (2010). Multiple-relaxation-time lattice Boltzmann model for the convection and anisotropic diffusion equation. *Journal of Computational Physics*, **229**(20), 7774–7795.

Yu, D., Mei, R., Luo, L., & Shyy, W. (2003). Viscous flow computations with the method of

lattice Boltzmann equation. *Progress in Aerospace Sciences*, **39**, 329–367.

Zhang, L., Yang, S., Zeng, Z., Chen, J., Wang, L., & Chew, J. W. (2017). A comparative study of the axisymmetric lattice Boltzmann models under the incompressible limit. *Computers and Mathematics with Applications*, **74**(4), 817–841.

Zhang, Y., Sun, C., Bao, Y., & Zhou, Q. (2018). How surface roughness reduces heat transport for small roughness heights in turbulent Rayleigh-Bénard convection. *Journal of Fluid Mechanics*, **836**, R2.

Zhu, X., Mathai, V., Stevens, R. J. A. M., Verzicco, R., & Lohse, D. (2018). Transition to the Ultimate Regime in Two-Dimensional Rayleigh-Bénard Convection. *Physical Review Letters*, **120**(14), 144502.

Zhu, X., Stevens, R. J. A. M., Verzicco, R., & Lohse, D. (2017). Roughness-Facilitated Local 1/2 Scaling Does Not Imply the Onset of the Ultimate Regime of Thermal Convection. *Physical Review Letters*, **119**(15), 1–5.